

Electronic Supporting Information

Dimeric tetrabromo-*p*-quinodimethanes: Synthesis and structural/electronic properties

Diego J. Vicent,^{a‡} Manuel Pérez-Escribano,^{b‡} Abel Cárdenas-Valdivia,^c A. Barragán,^d Joaquín Calbo,^b José I. Urgel,^d David Écija,^{*d} José Santos,^{*a} Juan Casado,^{*c} Enrique Ortí,^{*b} and Nazario Martín^{*ad}

^a*Departamento de Química Orgánica, Facultad de Ciencias Químicas, Universidad Complutense de Madrid, 28040 Madrid, Spain. E-mail: jsantosb@pdi.ucm.es; nazmar@quim.ucm.es*

^b*Instituto de Ciencia Molecular, Universidad de Valencia, 46980 Paterna, Spain. E-mail: enrique.orti@uv.es*

^c*Department of Physical Chemistry, University of Malaga, Campus de Teatines, 229071 Malaga, Spain. E-mail: casado@uma.es*

^d*IMDEA-Nanociencia, C/ Faraday, 9, Campus de Cantoblanco, 28049 Madrid, Spain.*

Corresponding authors: *jsantosb@ucm.es; enrique.orti@uv.es; nazmar@ucm.es*

[‡]*These authors have contributed equally*

Table of contents

S1. Experimental Section	3
S2. Stereoisomers Analysis	6
S3. NMR Spectra	7
S4. Mass Spectra	13
S5. Computational Methods	17
S6. Conformational analysis for TCAQ	18
S7. Frequency analysis of TBAQ conformations	19
S8. Stabilizing factors for TBAQ and TCAQ	21
S9. Rotational energy barriers for TBQ dimers	22
S10. Frontier molecular orbitals of TBQ1-5	25
S11. TD-DFT calculations of singlet excited states for TBQ1-5	27
S12. S_1 natural transition orbitals for TBQ1-5	30
S13. Effect of TBAQ torsion on the absorption spectra	32
S14. DFT benchmark	36
S15. Raman and IR experimental and calculated spectra	40
S16. On surface chemistry methods	54
S17. References	54

S1. Experimental section

General Experimental Details. All reactions were carried out under an argon atmosphere. Starting materials were purchased commercially and used as received. Compounds **2**,¹ **4**,² **5**³ and **8**⁴ were synthesised following previously reported methods. Solvents were dried using an Innovative Technology solvent purification system. TLC analysis was carried out using Merck Silica gel 60 F254 TLC plates and spots were visualized using a TLC lamp emitting at 365 or 254 nm. Silica gel column chromatography was performed using Fluorochem silica gel 60A, 40–63 micron. ¹H and ¹³C NMR spectroscopy was carried out on a Bruker Advance 300 (¹H: 400 MHz; ¹³C: 101 MHz) spectrometer at 298 K using partially deuterated solvents as internal standards. Coupling constants (*J*) are denoted in Hz and chemical shifts (δ) in ppm. Multiplicities are denoted as follows: s = singlet, d = doublet, t = triplet, m = multiplet. Residual solvent peaks were referenced as described in the literature⁵ and all NMR data was processed in MestReNova V11. FT-IR spectra were recorded on a Bruker Tensor 27 (ATR device) spectrometer. Melting points were carried out on a Stuart SMP40 machine with a ramping rate of 4 °C min⁻¹. The matrices used for MALDI-ToF were trans-2-[3-(4-*tert*-butylphenyl)-2-methyl-2-propenylidene]-malononitrile (DCTB) or 1,8-dihydroxy-9,10-dihydroanthracen-9-ona (dithranol) and mass analysis were performed in a Bruker Ultraflex II using a LTB MNL 106 laser source and/or a Maxis II using APCI ionization.

Electronic Absorption Spectroscopy Preliminary UV-Vis spectra were recorded in a Varian Cary 50 spectrophotometer, whereas the low temperature electronic absorption study was performed with a Cary 5000 UV-Vis-NIR spectrophotometer with superb photometric performance in the 175–3300 nm range. Tungsten halogen and deuterium arc excitation sources were employed for visible and UV, respectively. For reducing noise and stray light, a floating aluminium casting and a double Littrow monochromator were used. Detection range is extended into the NIR range by utilization of a PbSmart detector. Variable temperature electronic absorption spectra were obtained with an Optistat DN Oxford Instruments cryostat, which allows sample temperature variations from –196 °C to 200 °C. For this purpose, the employed solvent was 2-methyl-tetrahydrofuran (2Me-THF, Sigma- Aldrich/Merck, Anhydrous, ≥99%), since it provides a transparent frozen matrix at low temperatures.

2,2'-(buta-1,3-diyne-1,4-diy)bis(anthracene-9,10-dione) (**6**). In an oven-dried 25 mL round-bottom flask CuCl (5 mg, 0.05 mmol) and TMEDA (0.03 mL, 0.2 mmol) were suspended in dry DCM (15 mL). Upon addition of 2-ethynyl-6,13-anthracenedione (232 mg, 1 mmol), oxygen was bubbled into the resulting solution. The reaction was stirred protected from light overnight and the resulting yellow precipitate was filtered off and sequentially washed with a saturated solution of ammonium chloride (5 mL), water, MeOH, DCM and CHCl₃. The title product was isolated as a yellow solid (220 mg, 99%) and used without further purification. Lack of solubility in common deuterated solvents prevented from recording the NMR spectra of the compound. IR (ATR) $\bar{\nu}$: 1679 (C=O), 1588, 1294, 705 cm⁻¹; HRMS (APCI) *m/z*: calcd. for C₃₂H₁₄O₄ [M]⁺ 462.0887, found 462.0890; m.p: >300 °C.

2,2'-(1,4-phenylenebis(ethyne-2,1-diy))bis(anthracene-9,10-dione) (**7**). To an oven-dried 100 mL round-bottom flask were added Pd(PPh₃)₂Cl₂ (140 mg, 0.2 mmol), 1,4-diethynilbenzene (250 mg, 1.98 mmol) and 2-bromo-6,13-anthracenedione (**3**) (1140 mg, 3.96 mmol) under a N₂ blanket. After stirring for 5 min, dry deaerated Et₃N (60 mL) and CuI (40 mg, 0.4 mmol) were added under positive N₂ flow. After stirring overnight at 60 °C a precipitate was formed. Filtration and sequential washing with water, MeOH and DCM of the precipitate yielded a yellow solid (550 mg, 51%) that was used without further purification. Title compound's low

solubility in common organic solvents prevented registering the ^{13}C -NMR spectrum. ^1H -NMR (400 MHz, CDCl_3) δ : 8.46 (d, $J = 1.6$ Hz, 2H), 8.38–8.29 (m, 6H), 7.92 (dd, $J = 8.1, 1.6$ Hz, 2H), 7.84–7.82 (m, 4H), 7.61 (s, 4H) ppm. IR (ATR) $\bar{\nu}$: 1672 (C=O), 1588, 1279, 705 cm^{-1} ; HRMS (MALDI-TOF) m/z : calcd. for $\text{C}_{38}\text{H}_{19}\text{O}_4$ $[\text{M}+\text{H}]^+$ 538.1226, found 538.1205; m.p: >300 $^\circ\text{C}$.

TBQ1. To a solution of CBr_4 (610 mg, 1.84 mmol) in DCM (10 mL), PPh_3 (965 mg, 3.68 mmol) was added at 0 $^\circ\text{C}$, then 2,2-oxy-6,13-anthracenedione (**2**) (100 mg, 0.23 mmol) was added in one portion. The solution was stirred overnight at 40 $^\circ\text{C}$. Upon cooling to room temperature, the solvent was evaporated, and the resulting crude was crushed with MeOH (10 mL). The filtered solid was subjected to flash column chromatography using silica gel and hexane as eluent. The title product was isolated as a yellow solid (60 mg, 24%). ^1H -NMR (400 MHz, CDCl_3) δ : 7.91–7.74 (m, 6H), 7.49–7.42 (m, 2H), 7.36–7.28 (m, 4H), 7.01–6.90 (m, 2H) ppm; $^{13}\text{C}\{^1\text{H}\}$ -NMR (101 MHz, CDCl_3) δ : 155.4, 155.3, 139.1, 139.1, 139.0, 137.9, 137.7, 136.04, 136.02, 135.75, 135.71, 131.3, 131.2, 129.4, 129.3, 127.8, 127.8, 127.3, 127.28, 127.23, 127.17, 118.4, 118.0, 117.7, 117.4, 91.2, 91.1, 90.3, 90.28 ppm; IR (ATR) $\bar{\nu}$: 1561, 1463, 1230, 1222, 998, 763, 613 cm^{-1} ; HRMS (APCI) m/z : calcd. for $\text{C}_{32}\text{H}_{15}\text{Br}_8\text{O}$ $[\text{M}+\text{H}]^+$ 1046.4601; found 1046.4584; m.p: 105–107 $^\circ\text{C}$.

General procedure for the synthesis of TBQ2–5. The corresponding TBQ dimer (0.1 mmol, 1 equiv.) was dispersed into boiling dry THF (30 mL). Then, CBr_4 (1 mmol, 10 equiv.) and $\text{P}(\text{O}i\text{Pr})_3$ (2 mmol, 20 equiv.) were sequentially added. After stirring for 1 h, another load of CBr_4 and $\text{P}(\text{O}i\text{Pr})_3$ was added, and the process was repeated two more times until total conversion of the starting material. Upon cooling to room temperature, the solvent was evaporated, and the resulting crude was crushed with MeOH (30 mL), filtered and washed with MeOH. TBQ products were purified by column chromatography in silica gel, eluting with a Hex/ CHCl_3 (99:1) mixture.

TBQ2. The product was obtained as a white solid (64 mg, 60%). ^1H NMR (400 MHz, CDCl_3) δ : 8.00 (d, $J = 1.6$ Hz, 1H), 7.99 (d, $J = 1.6$ Hz, 1H), 7.87–7.79 (m, 6H), 7.42 (dd, $J = 8.1, 1.6$ Hz, 2H), 7.33–7.28 (m, 4H) ppm; ^{13}C NMR (101 MHz, CDCl_3) δ : 139.2, 138.9, 136.3, 135.98, 135.74, 135.72, 130.8, 130.78, 130.26, 130.22, 127.9, 127.8, 127.3, 122.0, 91.27, 91.13, 91.1, 90.09, 90.06 ppm; IR (ATR) $\bar{\nu}$: 3064, 1606, 1581, 1562, 1546, 1454, 936, 833, 761 cm^{-1} ; Raman (solid state at 298 K, 785 nm laser) $\bar{\nu}$: 2219, 2210, 1601, 1593, 1581, 1561 cm^{-1} ; HRMS (APCI) m/z : calcd. for $\text{C}_{34}\text{H}_{15}\text{Br}_8$ $[\text{M}+\text{H}]^+$ 1054.4635; found 1054.4653; m.p: 110–113 $^\circ\text{C}$.

TBQ3. The product was obtained as a white solid (61 mg, 55%). ^1H NMR (400 MHz, CDCl_3) δ : 8.11 (d, $J = 1.6$ Hz, 2H), 7.94 (d, $J = 8.1$ Hz, 2H), 7.91–7.84 (m, 4H), 7.68 (s, 4H), 7.56 (dd, $J = 8.2, 1.6$ Hz, 2H), 7.32–7.30 (m, 4H) ppm; ^{13}C NMR could not be achieved due to the poor solubility of the product. IR (ATR) $\bar{\nu}$: 3068, 1606, 1581, 1564, 1550, 1461, 937, 821, 763 cm^{-1} ; Raman (solid state at 298 K, 785 nm laser) $\bar{\nu}$: 1607, 1596, 1581, 1559 cm^{-1} ; HRMS (MALDI-TOF) m/z : calcd. for $\text{C}_{38}\text{H}_{18}^{79}\text{Br}_4^{81}\text{Br}_4$ $[\text{M}]^+$ 1113.4794, found 1113.4793. m.p: 125–129 $^\circ\text{C}$.

TBQ4. The product was obtained as a white solid (70 mg, 60%). ^1H NMR (400 MHz, CDCl_3) δ : 8.00 (d, $J = 1.6$ Hz, 2H), 7.88–7.81 (m, 6H), 7.51 (s, 4H), 7.44 (dd, $J = 8.1, 1.7$ Hz, 2H), 7.33–7.29 (m, 4H) ppm; ^{13}C NMR (101 MHz, CDCl_3) δ : 139.2, 138.9, 136.3, 135.9, 135.75, 135.73, 131.8, 130.7, 130.2, 128.0, 127.84, 127.81, 127.3, 123.2, 122.0, 91.2, 91.1, 90.9, 90.4 ppm; IR (ATR) $\bar{\nu}$: 3062, 2358, 1602, 1583, 1541, 1506, 1454, 937, 835, 763 cm^{-1} ; Raman (solid state at 298 K, 785 nm laser) $\bar{\nu}$: 2215, 1595, 1582, 1562 cm^{-1} ; HRMS (MALDI-TOF) m/z : calcd. for $\text{C}_{42}\text{H}_{18}^{79}\text{Br}_4^{81}\text{Br}_4$ $[\text{M}]^+$ 1161.4794, found 1161.4772; m.p: 112–118 $^\circ\text{C}$.

TBQ5. The product was obtained as a white solid (71 mg, 65%). ^1H NMR (400 MHz, CDCl_3) δ : 7.99 (d, $J = 1.7$ Hz, 2H), 7.87–7.79 (m, 6H), 7.43 (dd, $J = 8.1, 1.7$ Hz, 2H), 7.31 (dd, $J = 5.9, 3.3$ Hz, 4H) ppm; ^{13}C NMR (101 MHz, CDCl_3) δ : 139.1, 138.6, 136.8, 136.3, 135.6, 135.56, 131.6, 131.0, 128.0, 127.9, 127.8, 127.4, 120.6, 91.53, 91.50, 81.7, 75.1 ppm; IR (ATR) $\bar{\nu}$: 3064, 1600, 1593, 1583, 1562, 1541, 1460, 1454, 983, 937, 833, 765 cm^{-1} ; Raman (solid state at 298 K, 785 nm laser) $\bar{\nu}$: 2222, 2209, 1602, 1594, 1581, 1559 cm^{-1} ; HRMS (APCI) m/z : calcd. for $\text{C}_{36}\text{H}_{15}^{79}\text{Br}_4^{81}\text{Br}_4$ $[\text{M}+\text{H}]^+$ 1086.4558; found 1086.4575. m.p: 112–115 $^\circ\text{C}$.

S2. Stereoisomers analysis

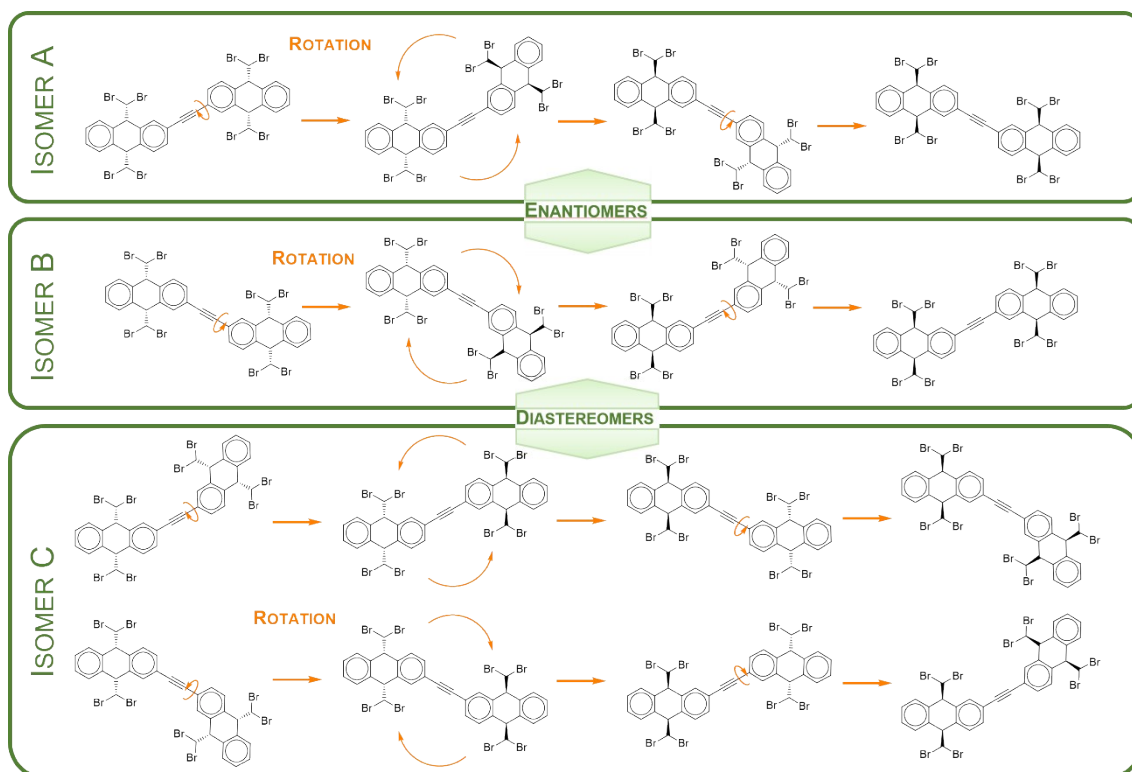


Figure S1. Stereoisomerism analysis of compound **TBQ2**, showing three possible stereoisomers: A and B being enantiomers, whereas C is a meso form. Orange arrows indicate possible rotations along the alkyne bridge or on-the-plane.

S3. NMR spectra

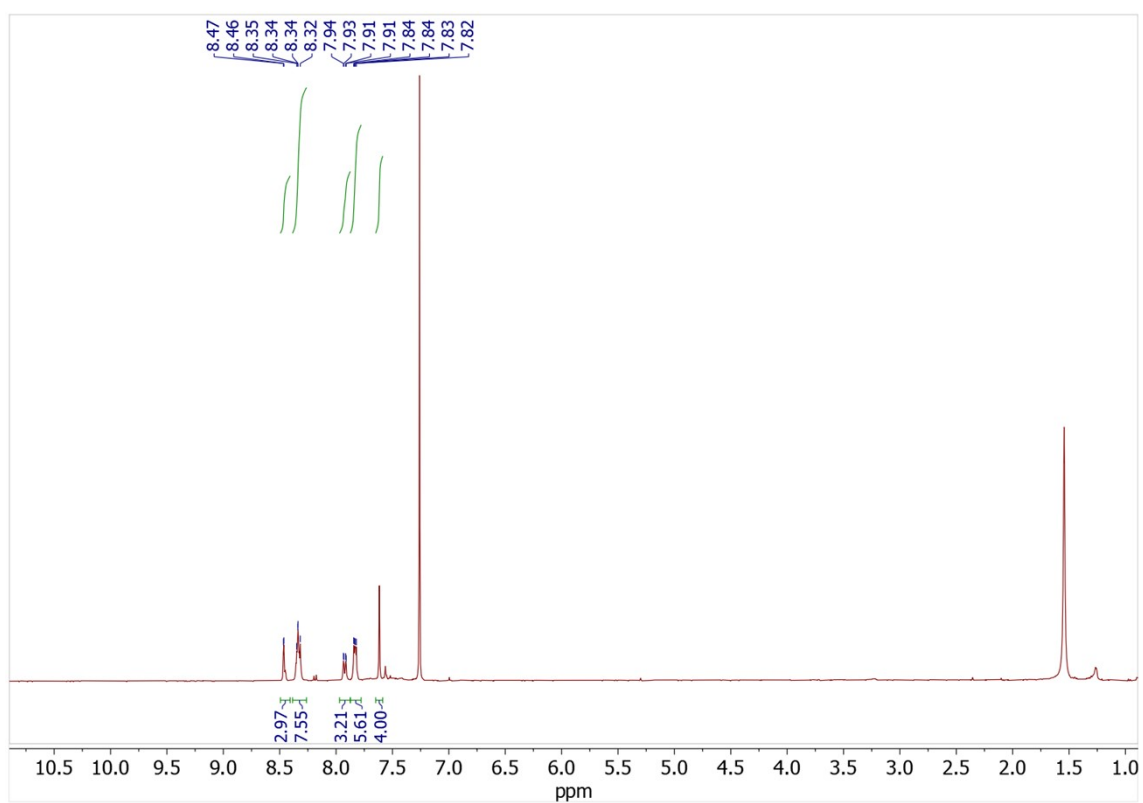


Figure S2. ¹H-NMR (400 MHz) spectrum of compound **7**, recorded in CDCl₃ at 25 °C.

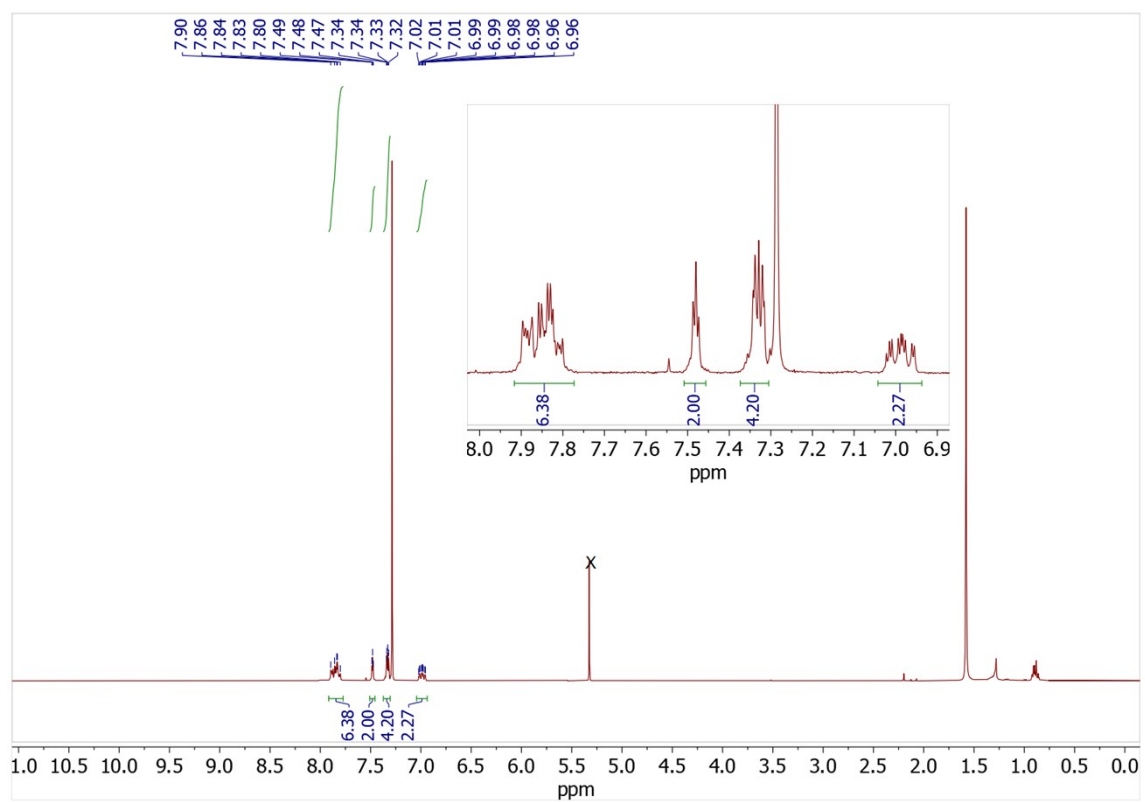


Figure S3. ¹H-NMR (400 MHz) spectrum of **TBQ1**, recorded in CDCl₃ at 25 °C.

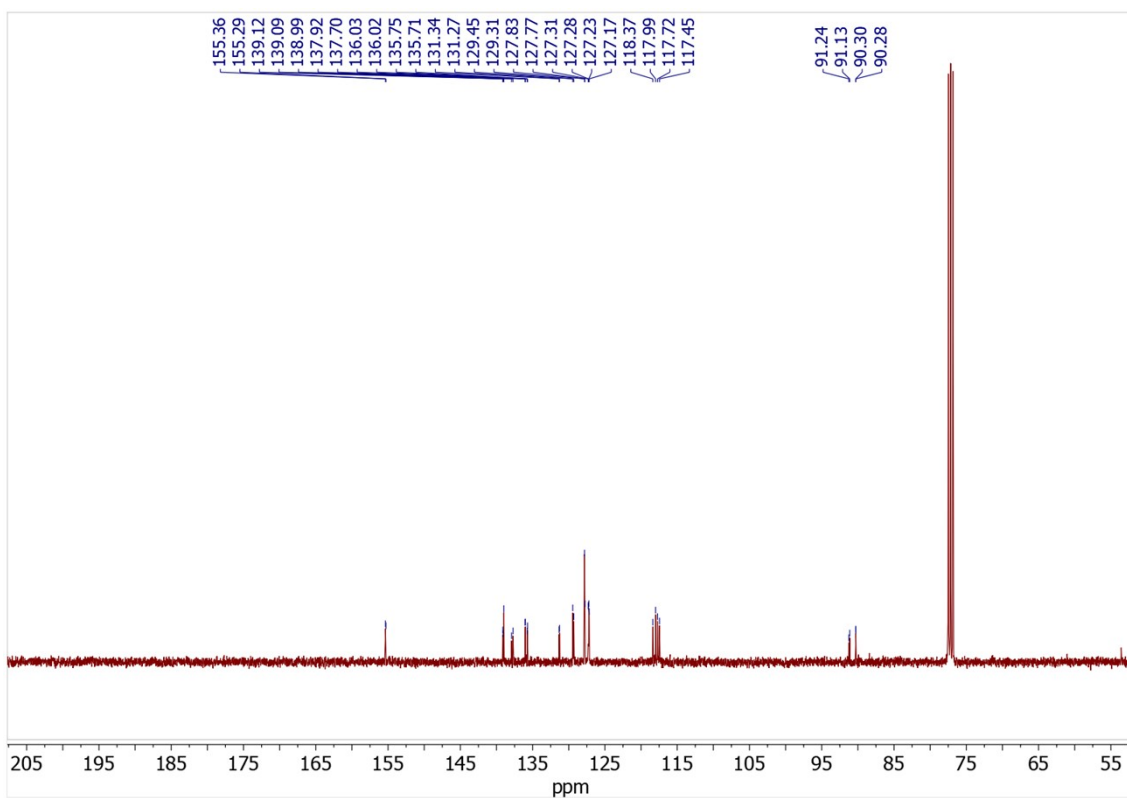


Figure S4. ^{13}C -NMR (101 MHz) spectrum of **TBQ1**, recorded in CDCl_3 at 25 °C.

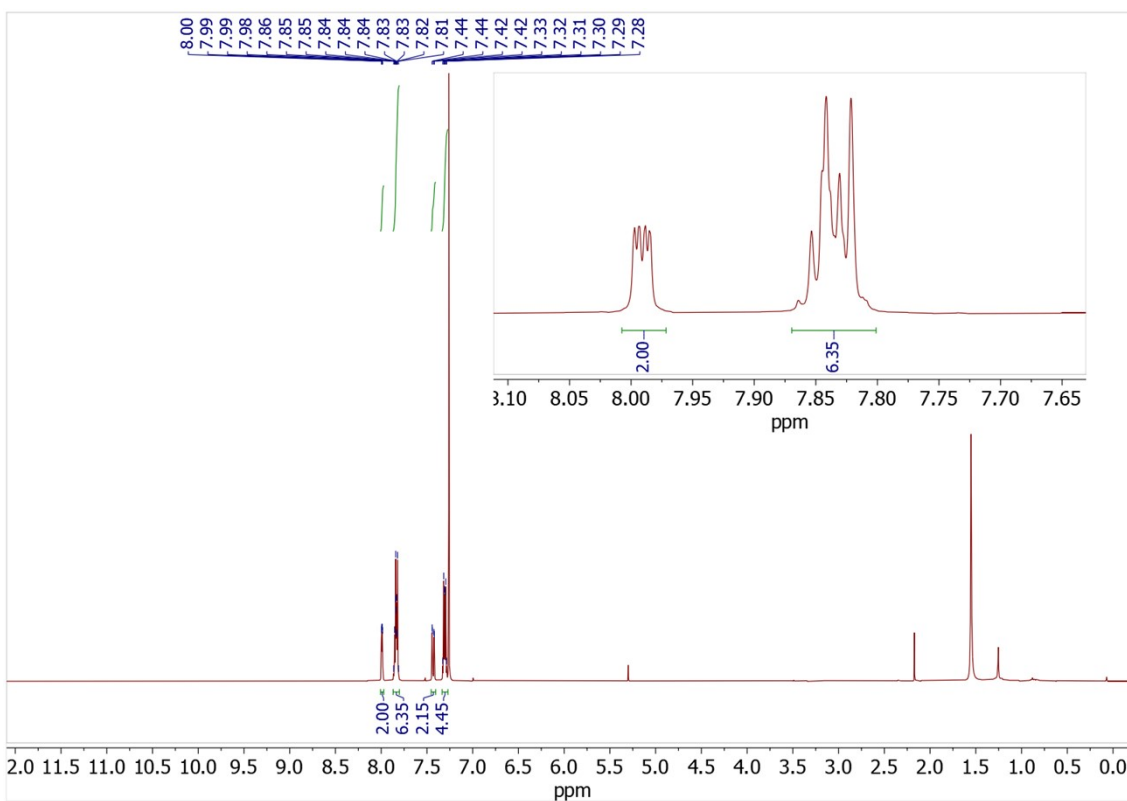


Figure S5. ^1H -NMR (400 MHz) spectrum of **TBQ2**, recorded in CDCl_3 at 25 °C.

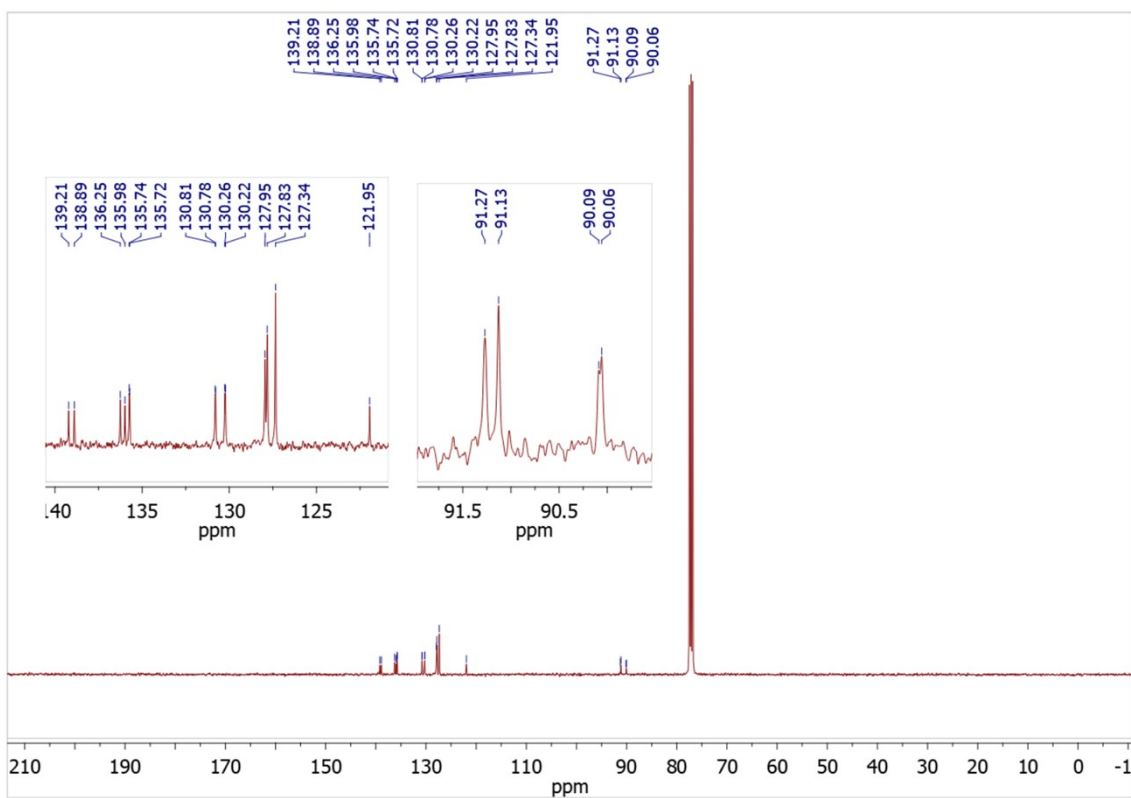


Figure S6. ^{13}C -NMR (101 MHz) spectrum of TBQ2, recorded in CDCl_3 at $25\text{ }^\circ\text{C}$.

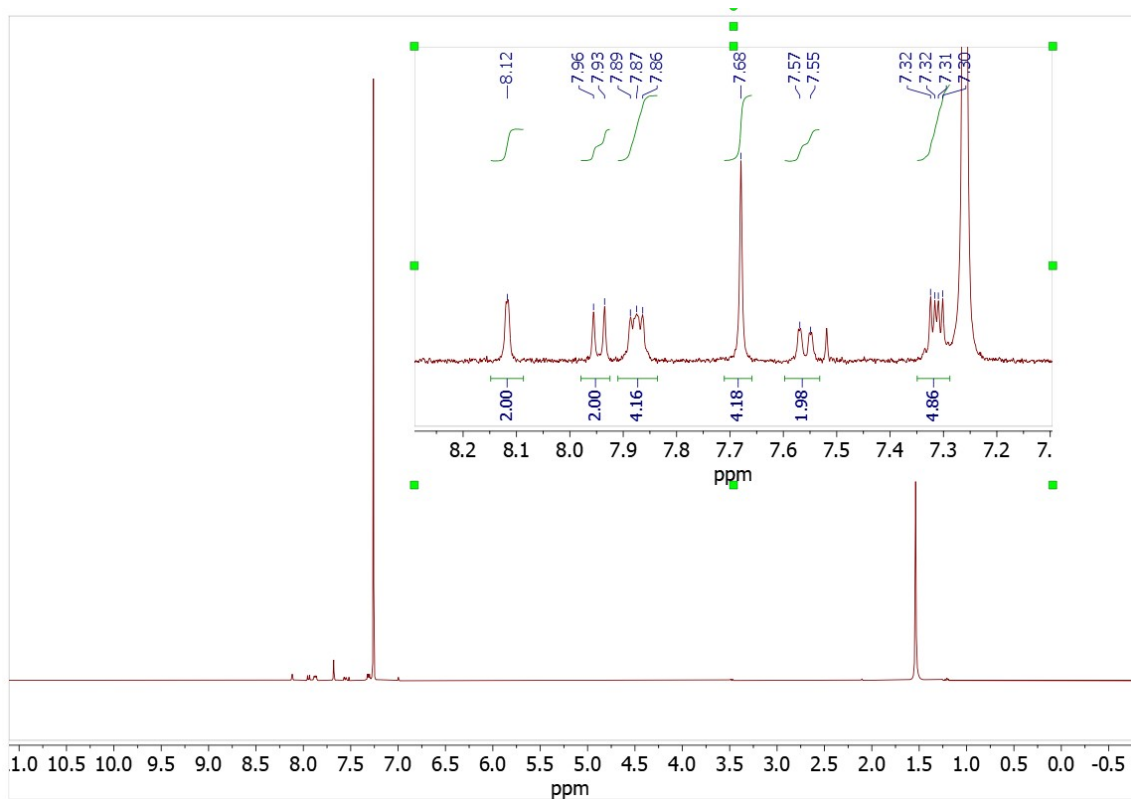


Figure S7. ^1H -NMR (400 MHz) spectrum of TBQ3, recorded in CDCl_3 at $25\text{ }^\circ\text{C}$.

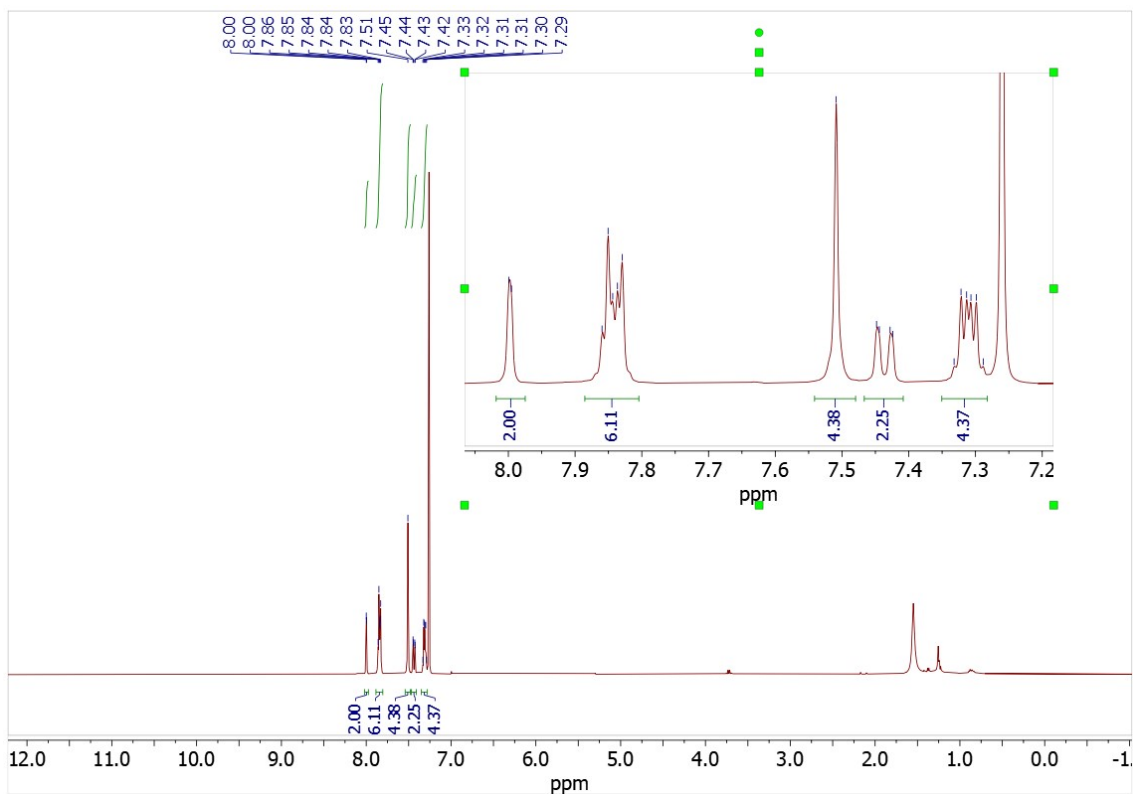


Figure S8. $^1\text{H-NMR}$ (400 MHz) spectrum of **TBQ4**, recorded in CDCl_3 at 25 °C.

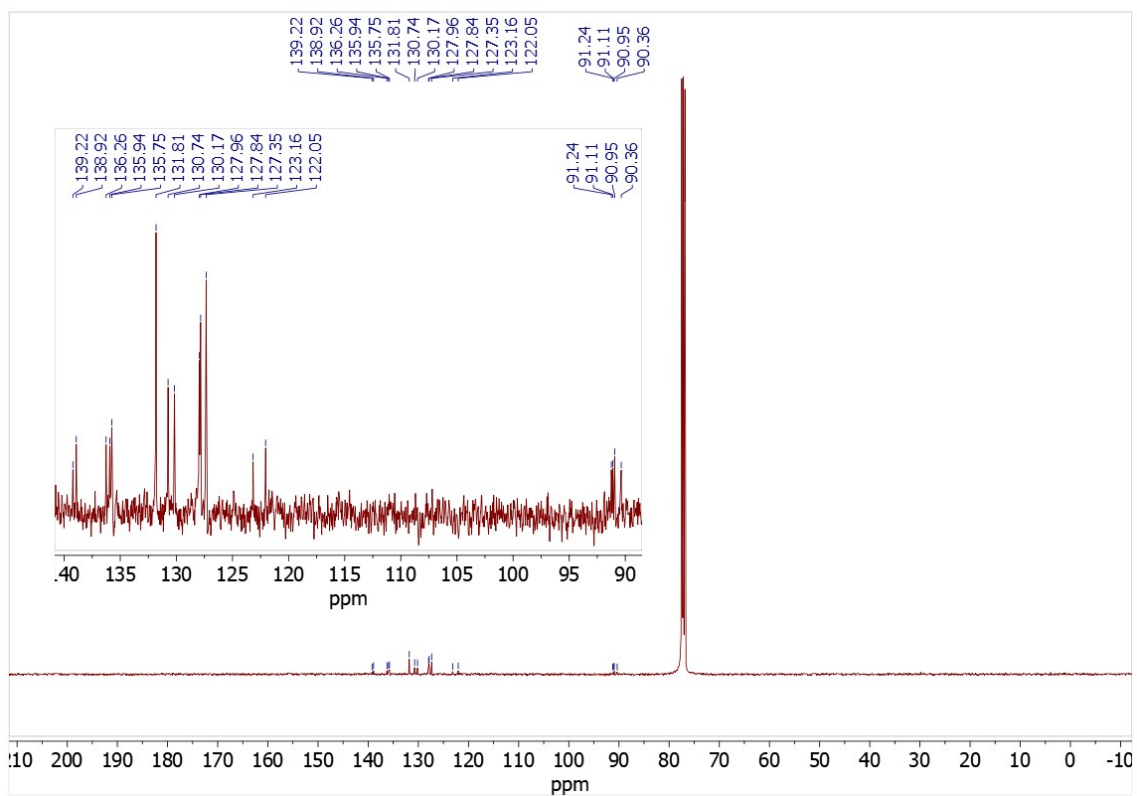


Figure S9. $^{13}\text{C-NMR}$ (101 MHz) spectrum of **TBQ4**, recorded in CDCl_3 at 25 °C.

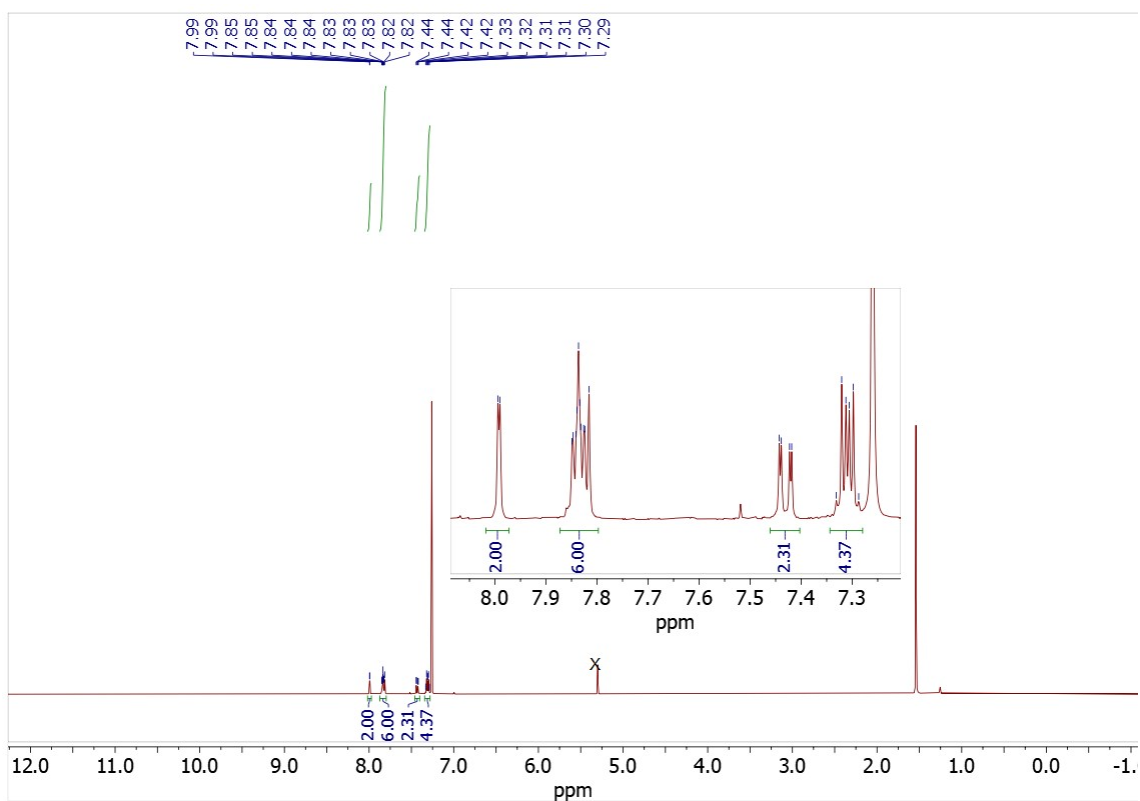


Figure S10. $^1\text{H-NMR}$ (400 MHz) spectrum of **TBQ5**, recorded in CDCl_3 at 25 °C.

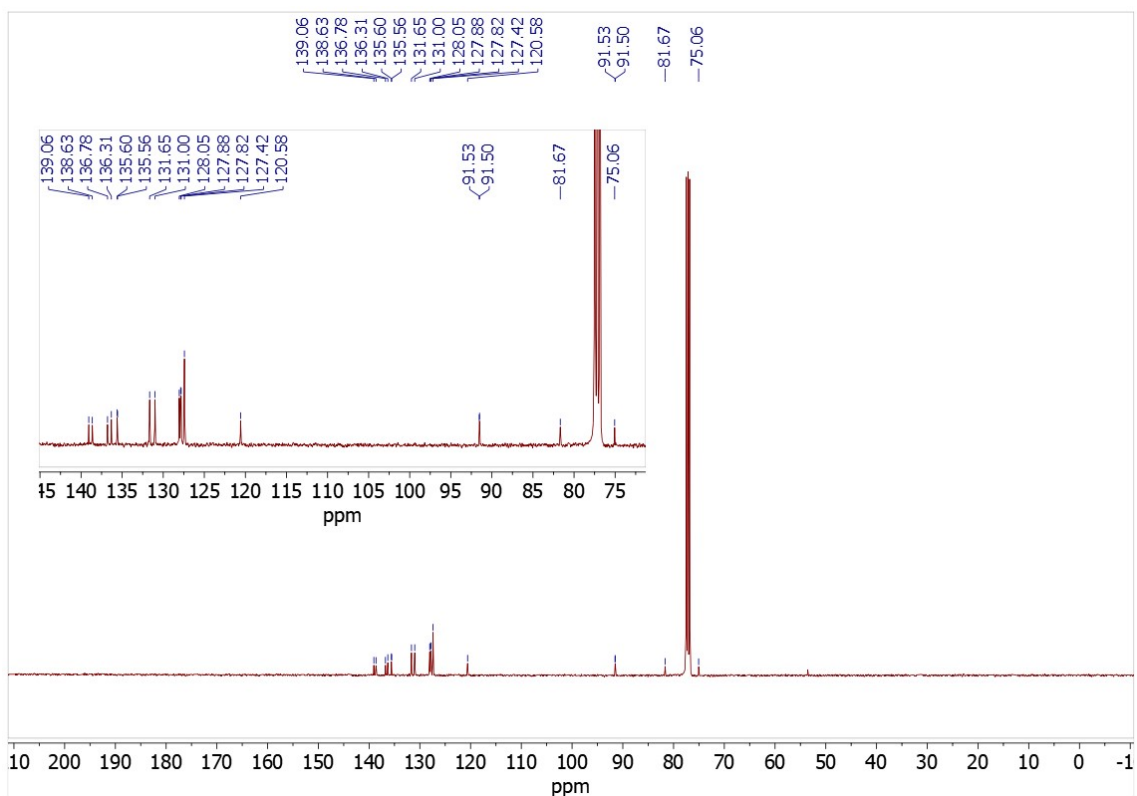


Figure S11. $^{13}\text{C-NMR}$ (101 MHz) spectrum of **TBQ5**, recorded in CDCl_3 at 25 °C.

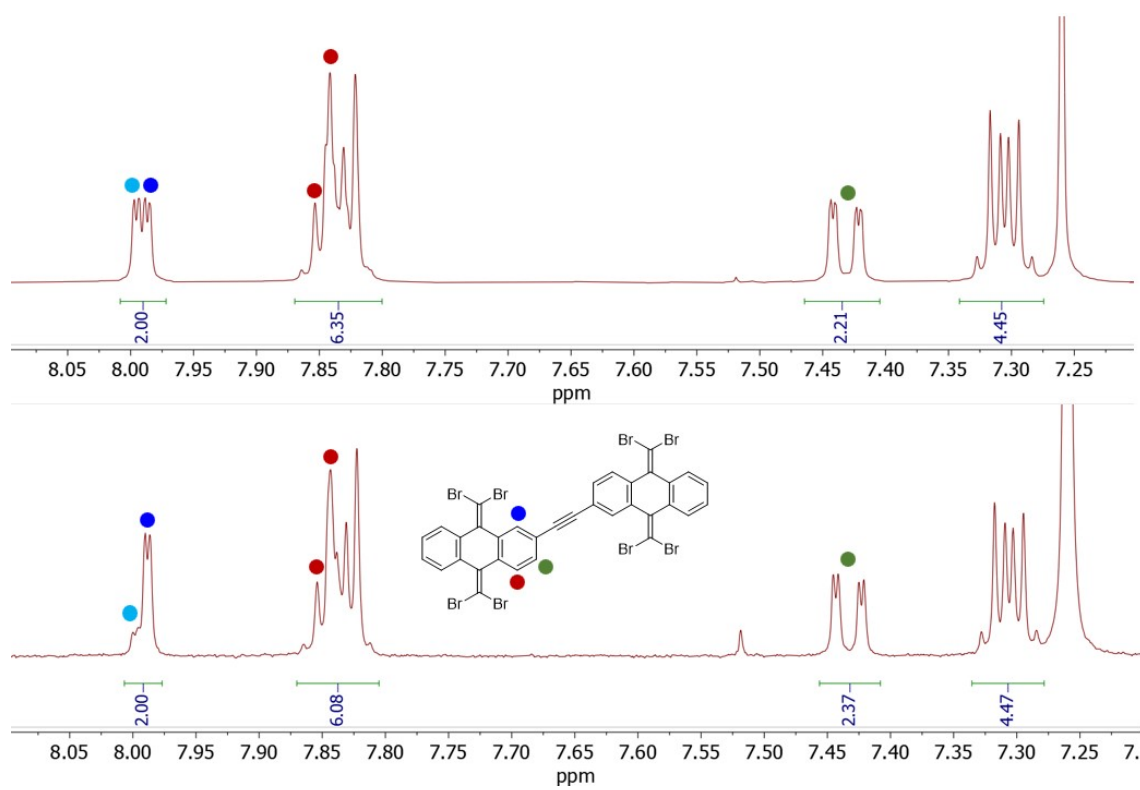


Figure S12. ¹H-NMR (400 MHz) spectra of **TBQ2**, recorded in CDCl₃ at 25 °C, as obtained after chromatographic purification (top) and after rinsing a solid sample with dichloromethane (below).

S4. Mass spectra

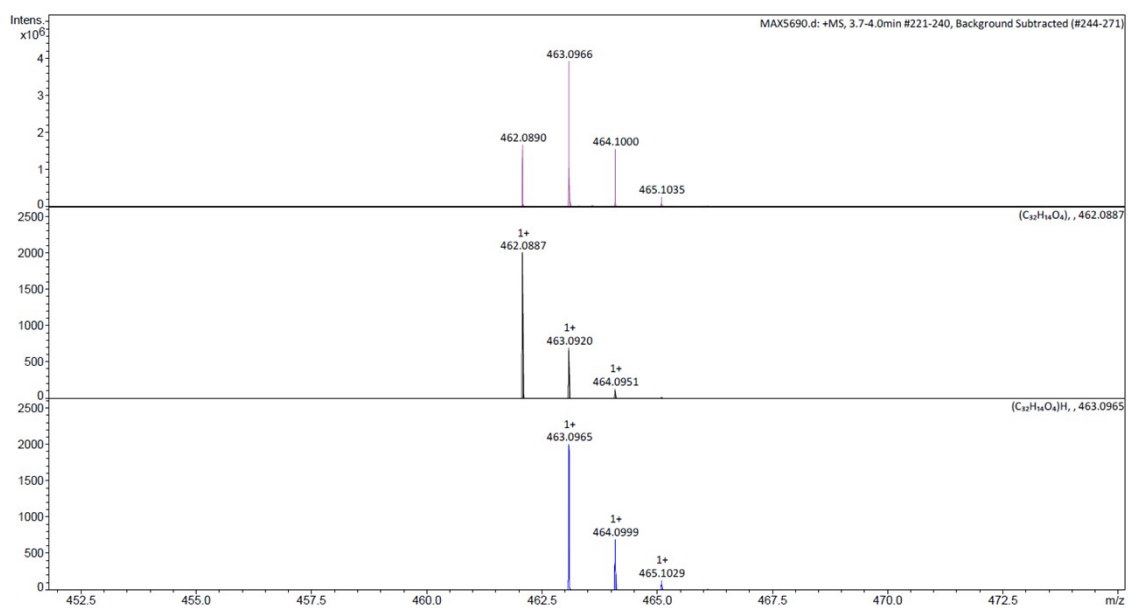


Figure S13. APCI-HRMS of compound 6.

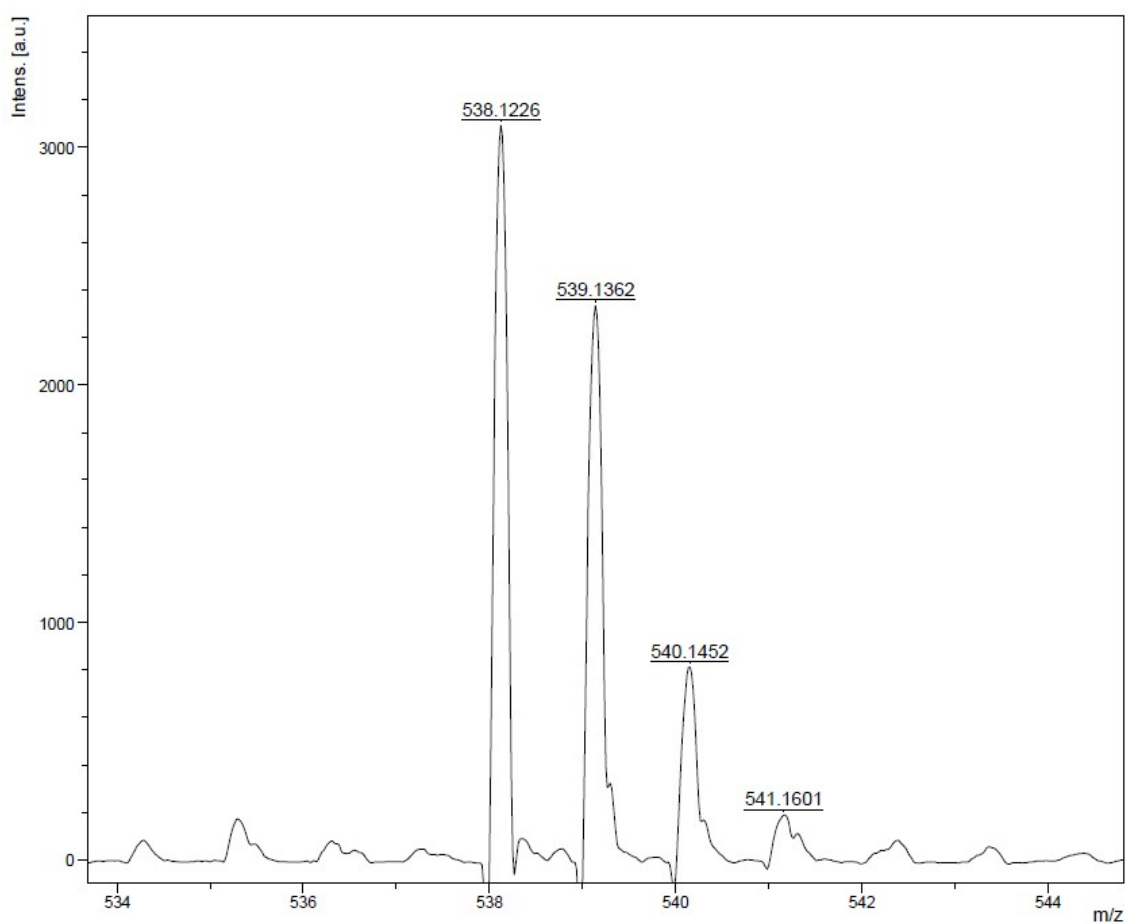


Figure S14. MALDI-HRMS of compound 7.

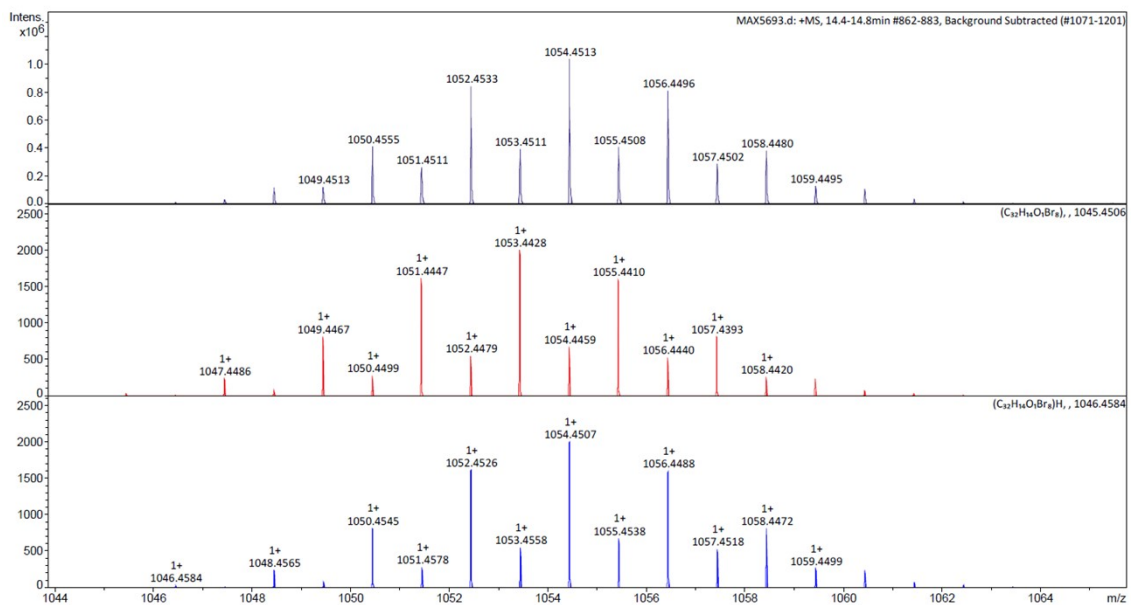


Figure S15. APCI-HRMS of compound TBQ1.

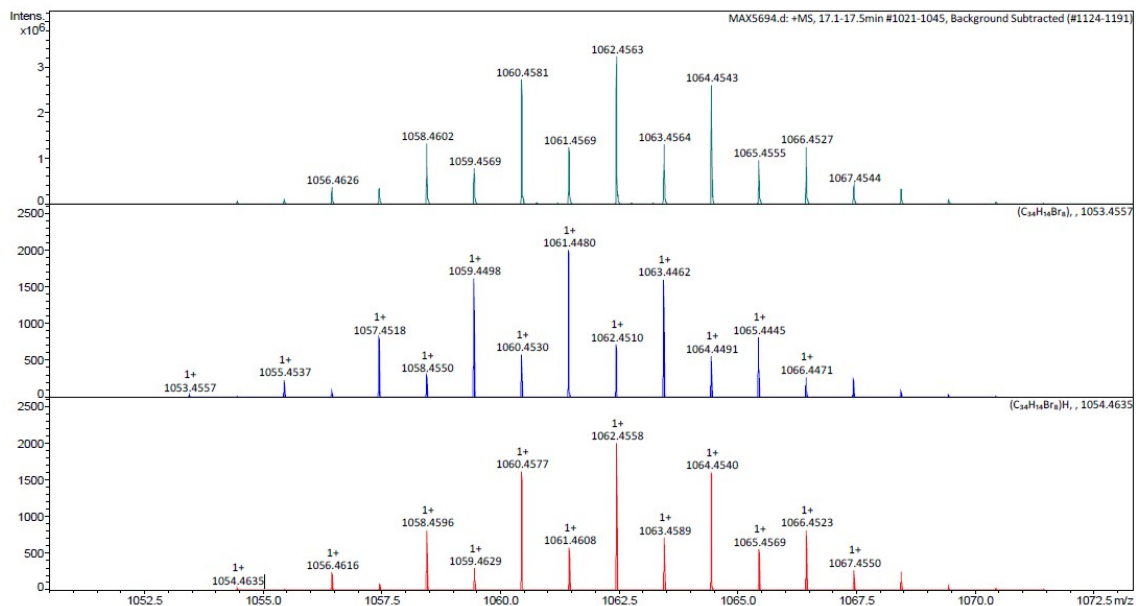


Figure S16. APCI-HRMS of compound TBQ2.

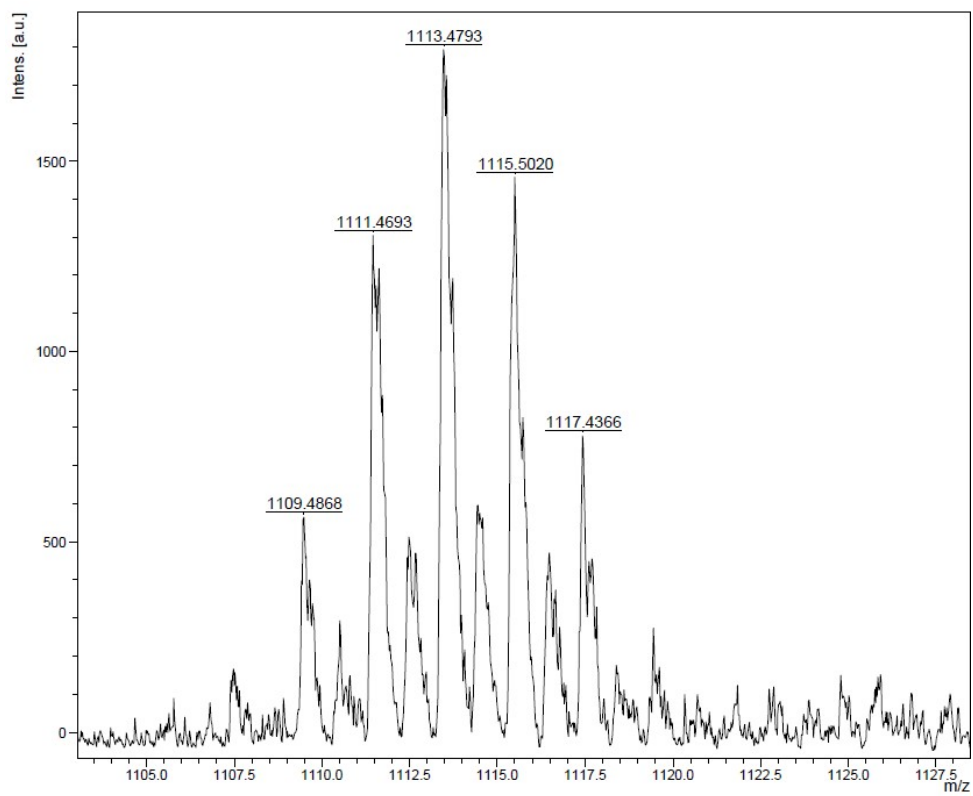


Figure S17. MALDI-HRMS of compound TBQ3.

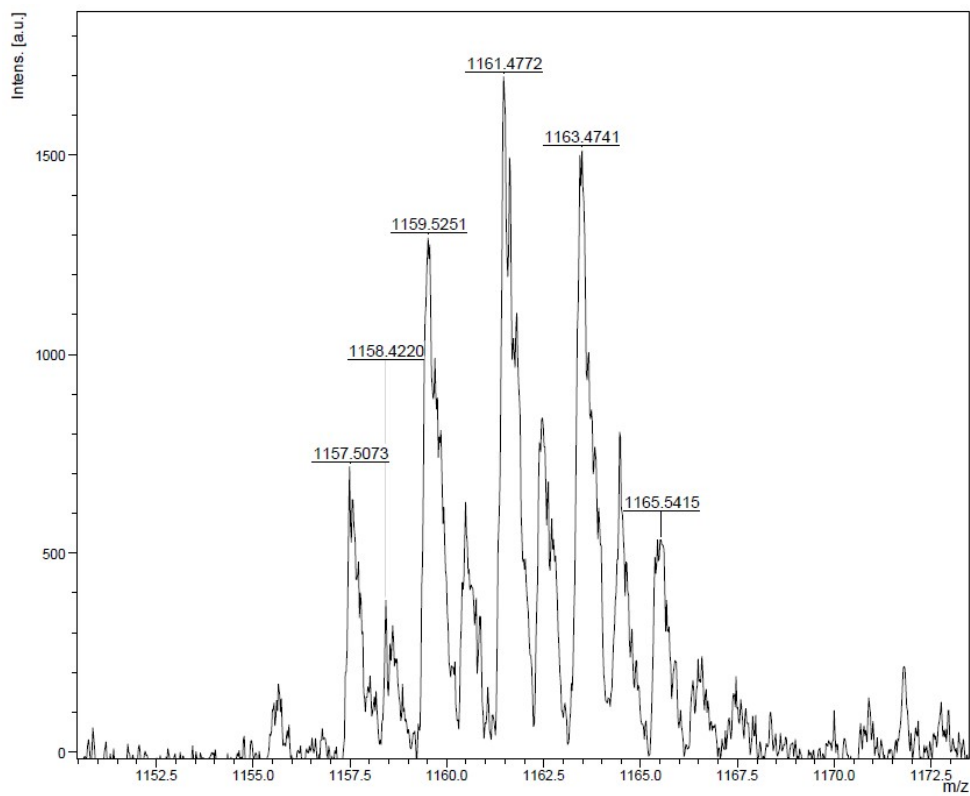


Figure S18. MALDI-HRMS of compound TBQ4.

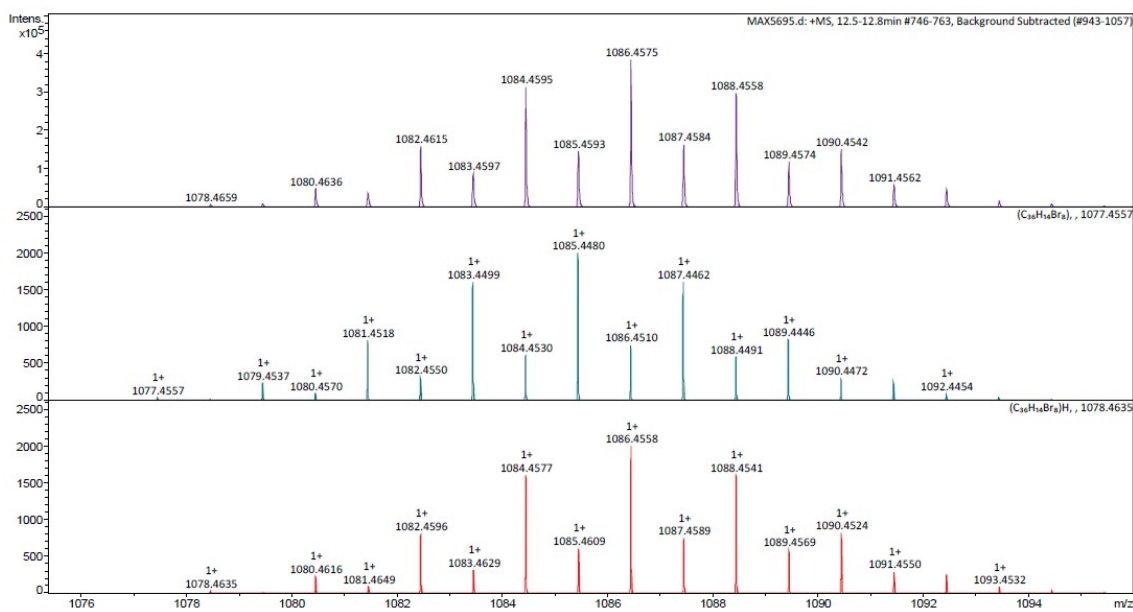


Figure S19. APCI-HRMS of compound TBQ5.

S5. Computational Methods

Theoretical calculations were performed under the density functional theory (DFT) and time-dependent DFT (TD-DFT) frameworks by making use of the Gaussian 16 suite of programs.⁶ All geometry optimizations and electronic structure calculations performed for **TCAQ**, **TBAQ** and **TBQ1–5**, except for the conformational analysis carried out for **TCAQ** and **TBAQ** and the simulation of the Raman spectra, included solvation effects by using the self-consistent reaction field (SCRF)⁷ approach and the polarizable continuum model (PCM).⁸ The solvent used was dichloromethane with a dielectric constant of $\epsilon = 8.93$. The functional employed was the τ -dependent gradient-corrected correlation BMK,⁹ which has proven successful to accurately describe the electronic levels of a wide variety of electroactive organic materials, and the Pople's 6-31G(d,p) basis set.^{10–14} The conformational analysis results using BMK as the DFT functional were benchmarked against those obtained with M06-2X¹⁵ and ω B97X-D¹⁶, as they were recently found to be accurate for isomer search and characterization¹⁷, and the standard B3LYP functional (see Section S14).¹⁸ The effect of the basis set enlargement was also inspected. Whereas the conformational analysis (stability electronic energy differences) was found very similar for all tested functionals, the well-known artificial over-delocalization from B3LYP led to an inaccurate description of the electronic excitations of **TBQ1–5**.¹⁹ For the convolution of the BMK/6-31G(d,p) simulated Raman spectra of the isolated molecules in gas phase (see Section S15), the vibrational frequencies were rescaled with a factor of 0.961, commonly used for B3LYP.²⁰ The BMK/6-31G(d,p) molecular structures for **TBAQ**, **TCAQ**, including all their isomers, as well as those for **TBQ1–5** calculated at the BMK/6-31G(d,p)+PCM(CH₂Cl₂) level are available for the reader[.]²¹

S6. Conformational analysis for TCAQ

The conformational analysis performed at the BMK/6-31G(d,p) level of theory in gas phase for the **TCAQ** molecule is very similar, both in terms of relative energies and symmetry of the different conformations, to that previously reported at PM3 and HF/6-31G* levels.^{22,23} The relative energies and molecular structures of the different conformations characterised as stationary points in the potential energy surface (PES) of **TCAQ** are schematically disclosed in Figure S20.

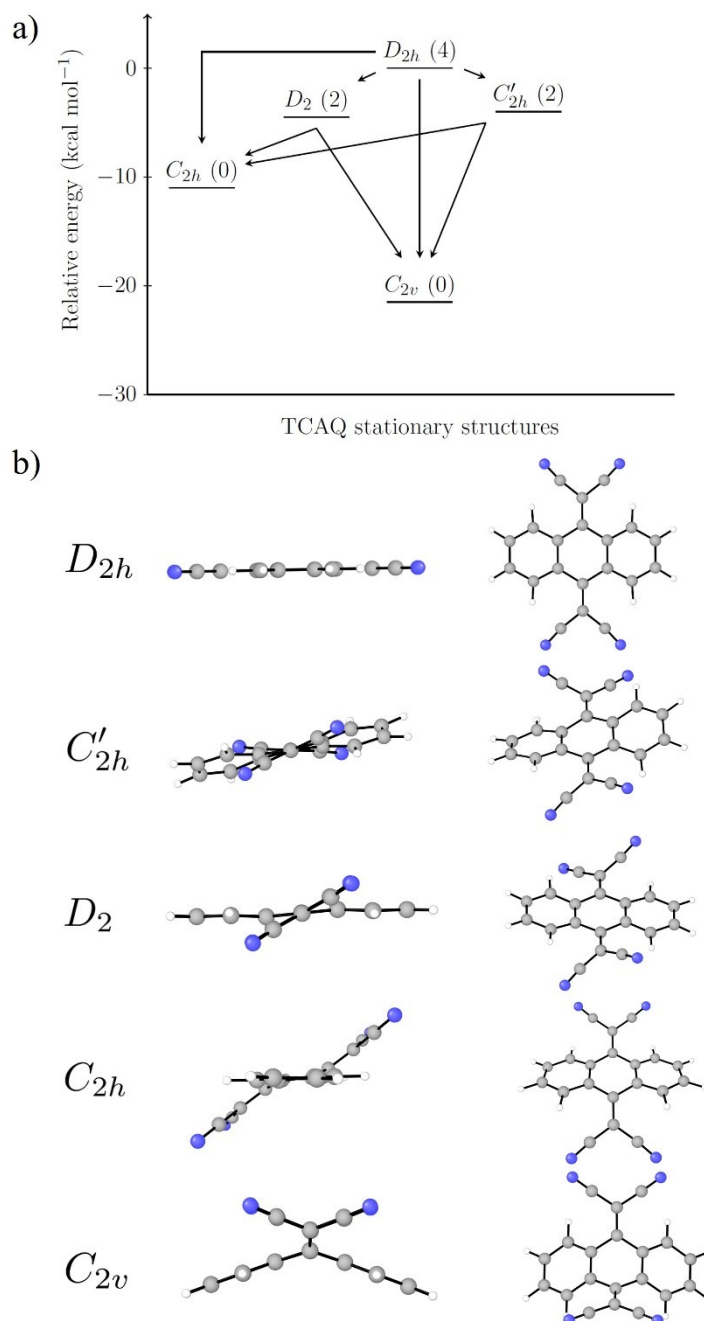


Figure S20. BMK/6-31G(d,p)-optimized relative electronic energies (a) and molecular structures (b) computed in gas phase for the different conformations characterized as stationary structures in the PES of **TCAQ**. In (a), the number of imaginary frequencies in each structure is indicated within parentheses, and the arrows indicate the evolution of the structure upon deformation along the imaginary modes. Color coding in (b): H in white, C in gray and N in blue.

S.7 Frequency analysis of TBAQ conformations

The five imaginary frequencies that arise in the gas phase BMK/6-31G(d,p) optimization of the **TBAQ** D_{2h} conformation are shown in Figure S21. Starting from this planar structure, the conformational analysis was done by distorting the molecular structure according to the vibrational modes and forcing the optimization to follow the symmetry point group of the resulting molecular geometries. If a stationary point was found along the optimization, the process was repeated from the new structure until all the frequencies calculated for the optimized structure were positive, thus pointing to a local minimum on the **TBAQ** ground state PES.

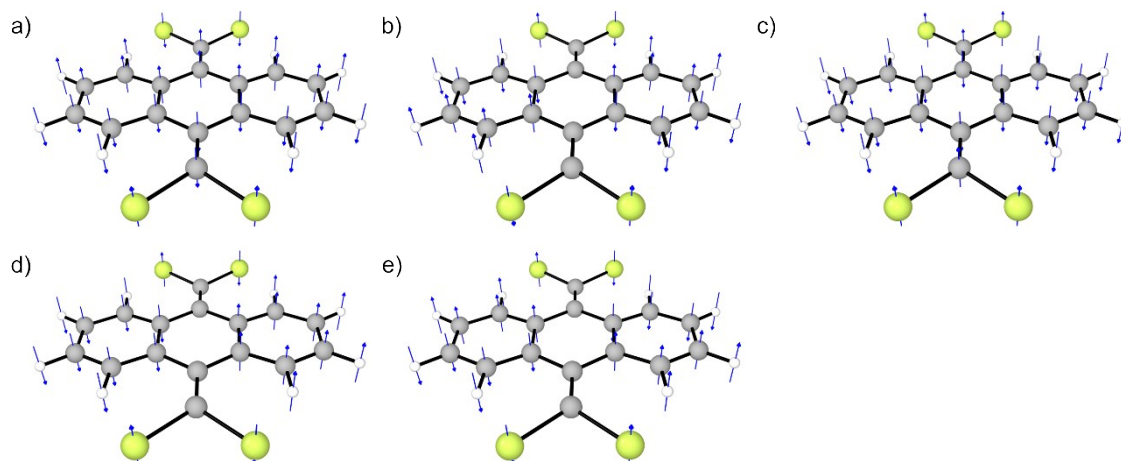


Figure S21. Imaginary-frequency vibrational modes computed for the **TBAQ** D_{2h} conformation, described by the blue arrows leading to the: a) C_{2h} , b) C'_{2h} , c) C_{2v} , d) D_2 and e) C^*_{2h} conformations.

As highlighted in Figure S21, three of the imaginary frequencies of the **TBAQ** D_{2h} conformation pointed to the transition states of C'_{2h} , D_2 and C^*_{2h} symmetry with 1, 2 and 1 imaginary frequencies, respectively. The imaginary frequencies of the C'_{2h} and C^*_{2h} conformations are disclosed in Figure S22 and Figure S23, respectively, while the two imaginary frequencies of the D_2 conformation are shown in Figure S24. Three out of these four imaginary frequencies pointed to the global C_{2v} minimum, while the second imaginary frequency of the D_2 structure pointed to the local C_{2h} minimum.

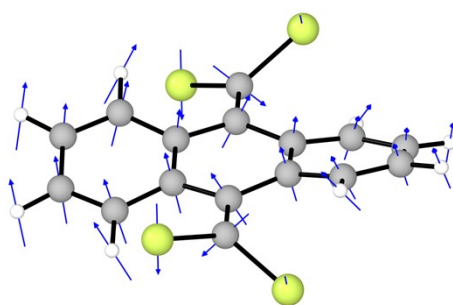


Figure S22. Imaginary frequency computed for the **TBAQ** C'_{2h} conformation, described by the blue arrows, that point to the C_{2v} conformation characterized as a true minimum.

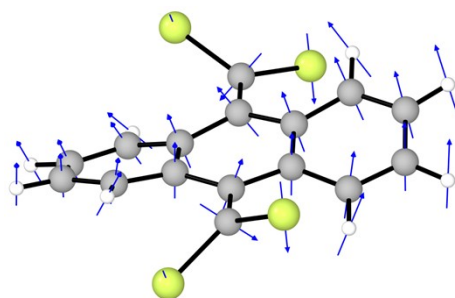


Figure S23. Imaginary frequency computed for the **TBAQ** C_{2h}^* conformation, described by the blue arrows, that point to the C_{2v} conformation characterized as a true minimum.

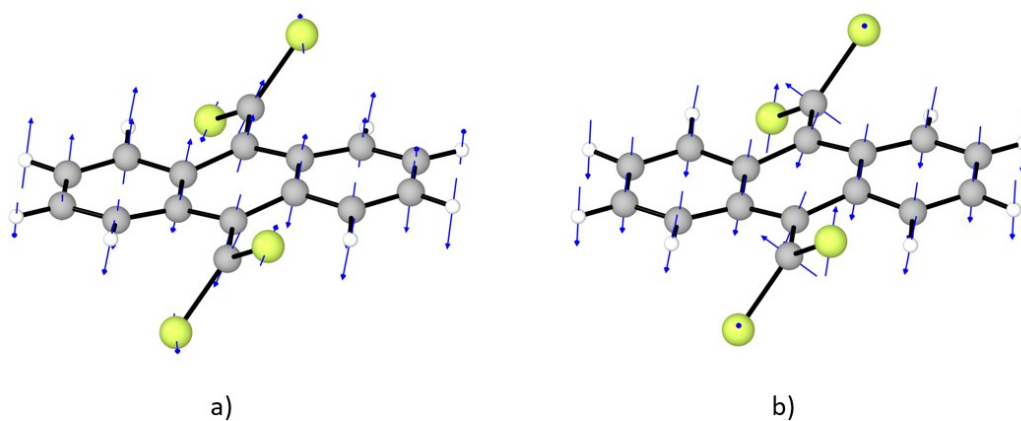


Figure S24. Imaginary frequencies computed for the **TBAQ** D_2 conformation, described by the blue arrows, that point to the a) C_{2h} and b) C_{2v} conformations characterized as true minima.

S8. Stabilizing factors for TBAQ and TCAQ

The stabilizing factors driving the structural changes from the planar D_{2h} conformation to the minimum-energy C_{2h} and C_{2v} conformations for both **TBAQ** and **TCAQ** molecules, whose values are disclosed in Table S1, were calculated at the BMK/6-31G(d,p) level of theory in gas phase. The computational procedure consisted in the following: 1) the *change in shape* factor, for both the D_{2h} -to- C_{2h} and D_{2h} -to- C_{2v} interconversion processes, is approximated by the electronic energy difference between the fully optimized D_{2h} structure and a single-point calculation on the C_{2h} or C_{2v} optimized structures using the bond lengths and angles of the D_{2h} structure, and 2) a second single-point calculation on the generated C_{2h} and C_{2v} structures but using the respective optimized bond lengths and angles for the Br–C–Br and CN–C–CN moieties to separately assess their effect. Remarkably, the broadening of the Br–C–Br and CN–C–CN angles plays an important role in the net stabilization upon interconversion to both C_{2h} and C_{2v} structures. The electron localization function (ELF) calculated for both **TCAQ** and **TBAQ** molecules is shown in Figure S25.

Table S1. Stabilization factors driving the interconversion from the planar D_{2h} conformation to the C_{2h} and C_{2v} minima for both **TBAQ** and **TCAQ**.

Relative energy to planar D_{2h} structure (kcal mol ⁻¹)		
Stabilization factor $D_{2h} \rightarrow C_{2h}$	TBAQ	TCAQ
Change in shape	-22.28	-5.52
+ Br–C–Br / CN–C–CN relaxation	-31.05	-10.14
Stabilization factor $D_{2h} \rightarrow C_{2v}$	TBAQ	TCAQ
Change in shape	-37.41	-10.67
+ Br–C–Br / CN–C–CN relaxation	-53.53	-21.77

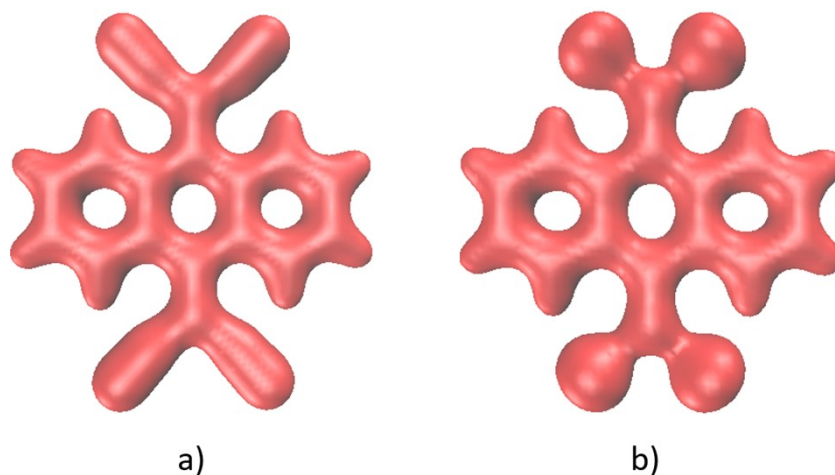


Figure S25. Electron localization function (ELF) calculated for **TCAQ** (a) and **TBAQ** (b) using the TopChem2 program.²⁴

S9. Rotational energy barriers for TBQ dimers

The rotation barrier profiles for **TBQ1** and **TBQ3–5** are shown in Figures S26–S29, alongside with the dihedral angles that were defined for the constrained exploration of the PES of the TBQ derivatives. The torsional profile of **TBQ2** is shown in Figure 3 in the main text. Table S2 provides the torsion barriers computed for **TBQ1–5**. For **TBQ2**, **TBQ4**, and **TBQ5**, the torsion barrier was calculated as the electronic energy difference between the molecular structure with highest energy along the rotation profile and that corresponding to a dihedral angle of 0° . For **TBQ1** the barrier was calculated as the energy difference between the structure at 0° , which presents the maximum energy, and the minimum-energy structure along the torsion (dihedral of 200°). For **TBQ3**, the energy barrier was calculated using the minimum energy structure located at a dihedral value of 120° and that with the highest energy at 60° .

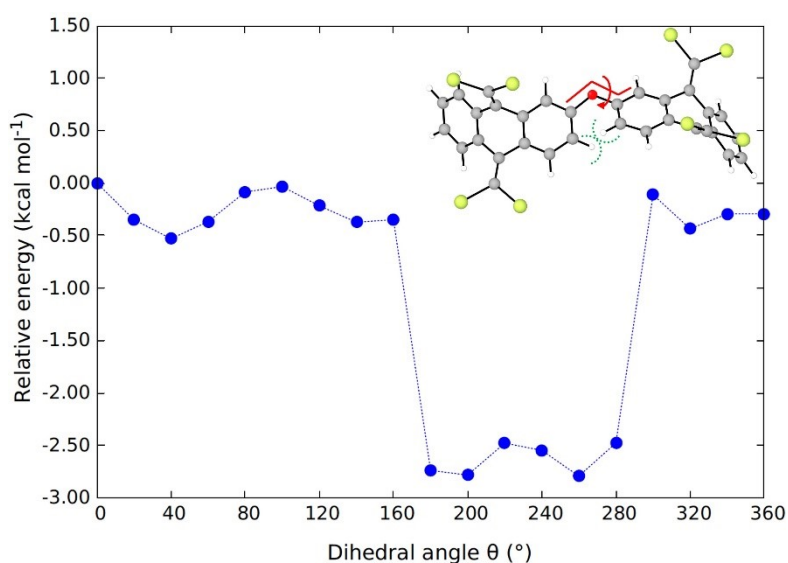


Figure S26. Rotational energy barrier profile calculated for **TBQ1** at the BMK/6-31(d,p)+PCM(CH₂Cl₂) level along the torsion of the dihedral angle θ shown in red.

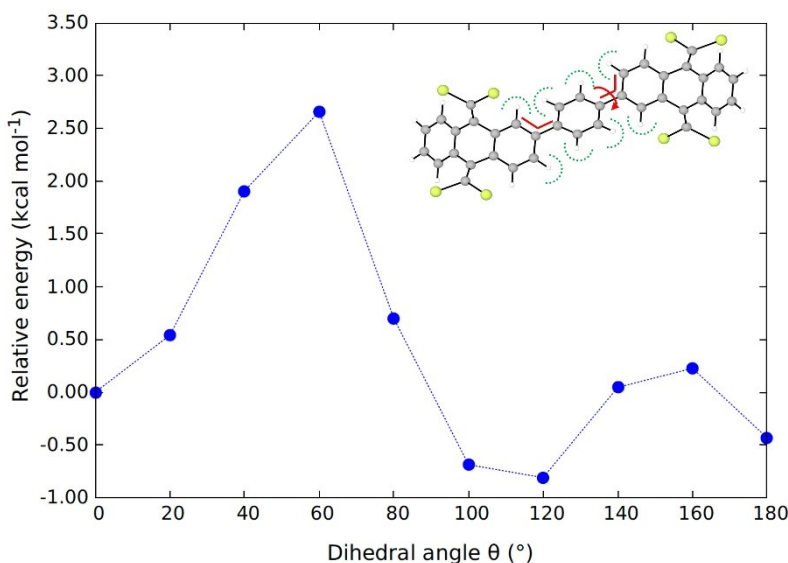


Figure S27. Rotational energy barrier profile of **TBQ3** calculated at the BMK/6-31(d,p)+PCM level in dichloromethane along the torsion of the dihedral angle θ shown in red.

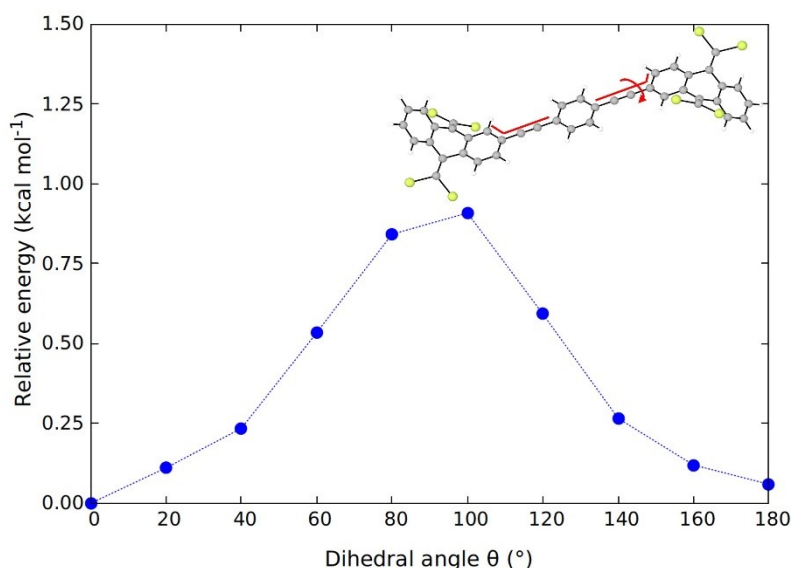


Figure S28. Rotational energy barrier profile of **TBQ4** calculated at the BMK/6-31(d,p)+PCM level in dichloromethane along the torsion of the dihedral angle θ shown in red.

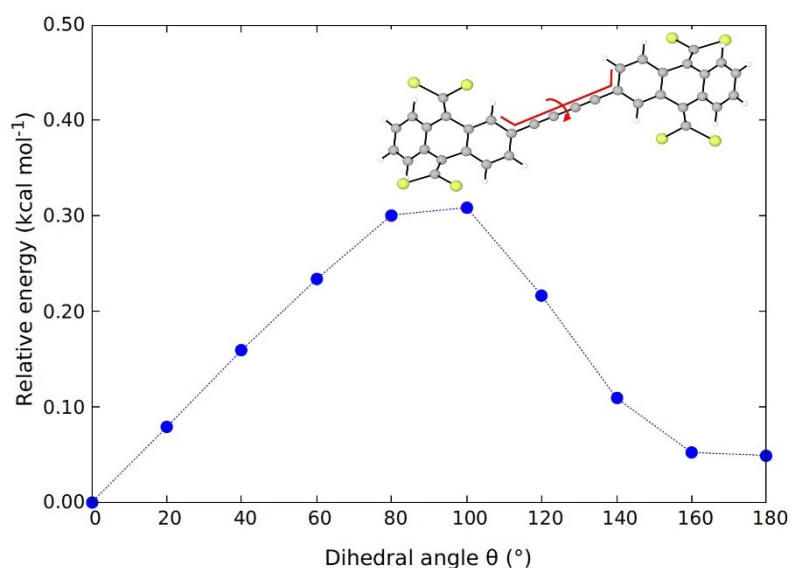


Figure S29. Rotational energy barrier profile of **TBQ5** calculated at the BMK/6-31(d,p)+PCM level in dichloromethane along the torsion of the dihedral angle θ shown in red.

Table S2. BMK/6-31G(d,p)+PCM(CH₂Cl₂) torsion barriers computed for **TBQ1–5**.

Dimer	Torsion barrier (kcal mol ⁻¹)
TBQ1	2.79
TBQ2	0.94
TBQ3	3.47
TBQ4	0.91
TBQ5	0.31

The Br...H–C1 distance (see Figure S30) was inspected along the rotation profile for **TBQ1–5** in order to explore the differences in the chemical environment of the *peri* proton resulting from the torsion of the **TBAQ-to-TBAQ** dihedral angle. The values of the distances for the different points of the rotational space explored are listed in Table S3.

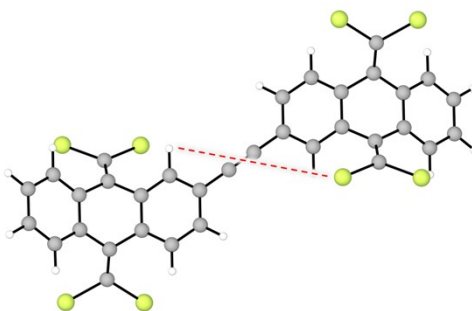


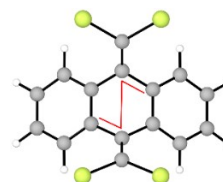
Figure S30. Br...H-C1 distance shown in red for **TBQ2**. The values of the distance for **TBQ1–5** along the rotation profile are listed in **Table S3**.

Table S3. Br...H-C1 distances (in Å) calculated for **TBQ1–5** along the rotation profile.

Dihedral angle (°)	TBQ1	TBQ2	TBQ3	TBQ4	TBQ5
0	6.75	8.34	9.62	13.93	10.26
20	7.88	8.50	9.80	14.00	10.40
40	8.34	8.48	9.80	14.04	10.41
60	8.58	8.35	10.78	13.96	10.30
80	8.76	8.08	10.53	13.71	10.03
100	8.89	7.71	10.31	13.66	9.71
120	8.89	7.34	10.19	13.39	9.49
140	8.73	6.87	9.95	13.11	9.09
160	8.36	6.49	10.31	12.68	8.82
180	7.38	6.17	10.26	12.67	8.53
200	7.44				
220	6.82				
240	6.21				
260	5.71				
280	5.31				
300	5.12				
320	5.30				
340	5.50				
360	5.83				

Table S4. Root-mean-square deviation (RMSD, in Å) of the atomic positions of the **TBAQ** units in **TBQ1–5** dimers compared to the **TBAQ** minimum-energy C_{2v} structure, and values of the dihedral angle (shown in red) showcasing the folding of the anthracene core of the **TBAQ** units.

System	RMSD (vs TBAQ C_{2v})	Dihedral angle (°) ^a
TBQ1	0.007	136.3
TBQ2	0.007	136.2
TBQ3	0.010	136.1
TBQ4	0.008	136.1
TBQ5	0.008	136.3



^aThe folding dihedral angle for **TBAQ** is calculated to be 136.3°.

S10. Frontier molecular orbitals of TBQ1–5

Figure S31 shows the atomic composition calculated at the BMK/6-31G(d,p)+PCM(CH₂Cl₂) level for the frontier molecular orbitals (FMOs) of **TBQ1–5**. The energies of the HOMO and LUMO of **TCAQ**, **TBAQ** and **TBQ1–5** dimers are listed in Table S5 and are shown for comparison as a diagram in Figure S32.

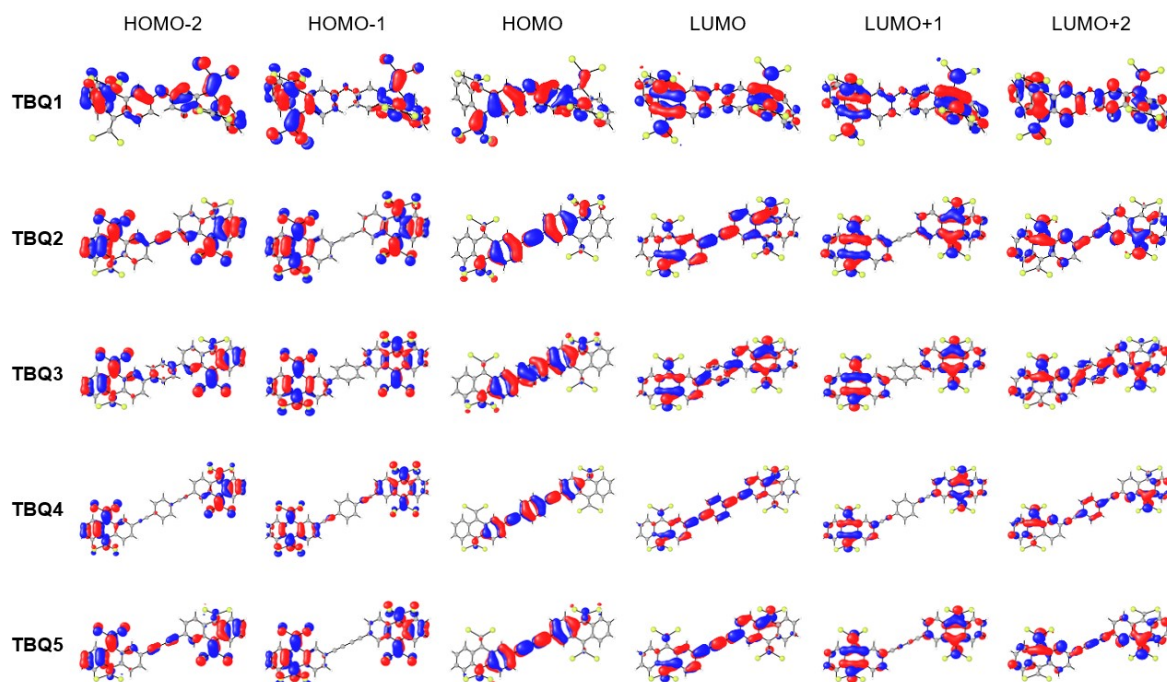


Figure S31. Frontier molecular orbitals of **TBQ1–5**.

Table S5. HOMO and LUMO energies, and HOMO–LUMO energy gap calculated at the BMK/6-31G(d,p)+PCM(CH₂Cl₂) level for **TCAQ**, **TBAQ** and **TBQ1–5**.

Species	HOMO energy (eV)	LUMO energy (eV)	H-L energy gap (eV)
TCAQ	-7.71	-3.49	4.22
TBAQ	-6.93	-1.18	4.89
TBQ1	-6.81	-1.34	5.47
TBQ2	-6.69	-1.68	5.01
TBQ3	-6.70	-1.45	5.25
TBQ4	-6.43	-1.75	4.69
TBQ5	-6.66	-1.82	4.84

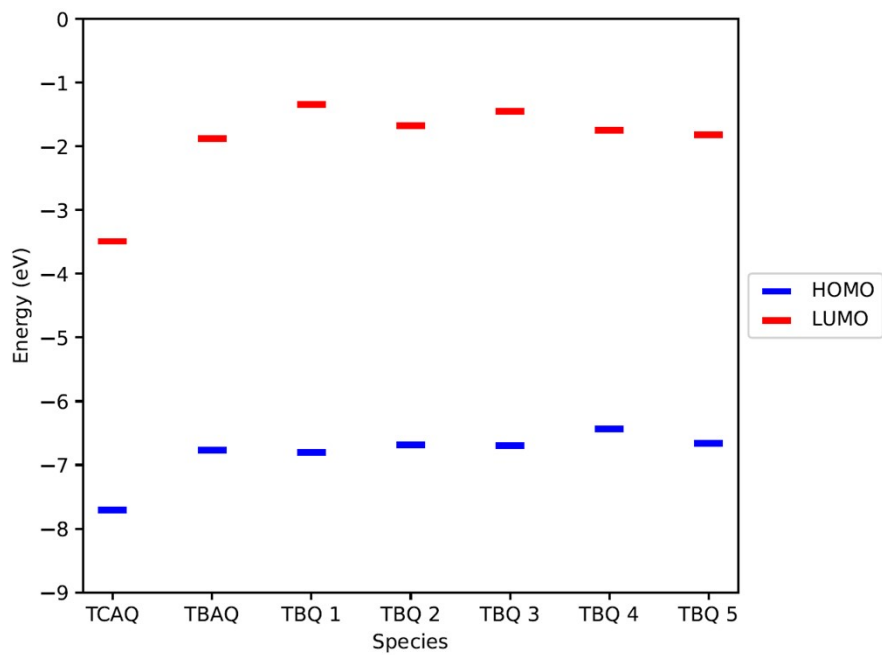


Figure S32. HOMO and LUMO energy diagram of **TCAQ**, **TBAQ** and **TBQ1-5**.

S11. TD-DFT calculations of singlet excited states for TBQ1–5

Singlet excited states (S_n) of **TBQ1–5** were computed at the BMK/6-31G(d,p)+PCM(CH_2Cl_2) level using TD-DFT calculations and the optimized geometry of the ground electronic state (S_0). The contribution of each singlet excited state to the absorption spectra of **TBQ1–5** is shown in Figures S33–S37, respectively. The description of the first two bright $S_0 \rightarrow S_n$ electronic transitions in terms of the molecular orbitals involved in them, alongside with their oscillator strength, are listed in Table S6. The wavelength of the calculated $S_0 \rightarrow S_1$ electronic transition, compared to the experimentally values of the lowest-energy absorption band, are detailed in Table S7.

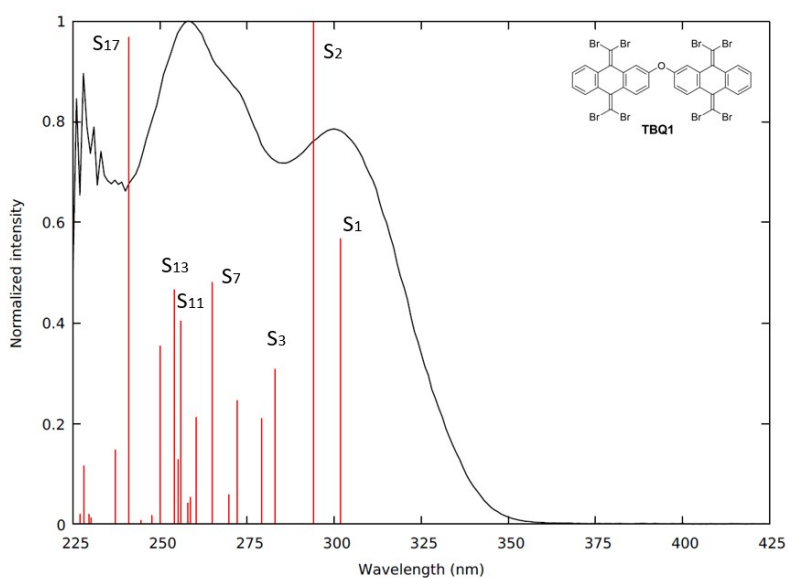


Figure S33. Experimental absorption spectra of **TBQ1** (black) and normalized oscillator strengths (red) of the calculated singlet excited states (S_n).

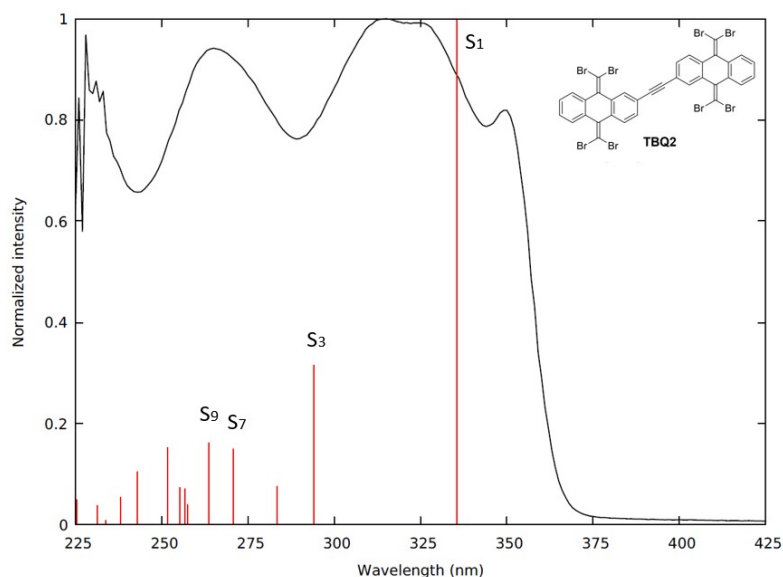


Figure S34. Experimental absorption spectra of **TBQ2** (black) and normalized oscillator strengths (red) of the calculated singlet excited (S_n) states.

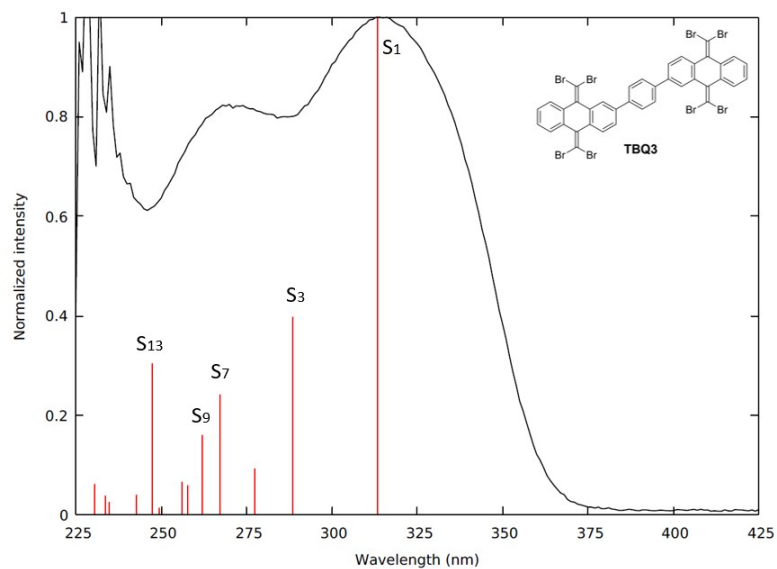


Figure S35. Experimental absorption spectra of **TBQ3** (black) and normalized oscillator strengths (red) of the calculated singlet excited (S_n) states.

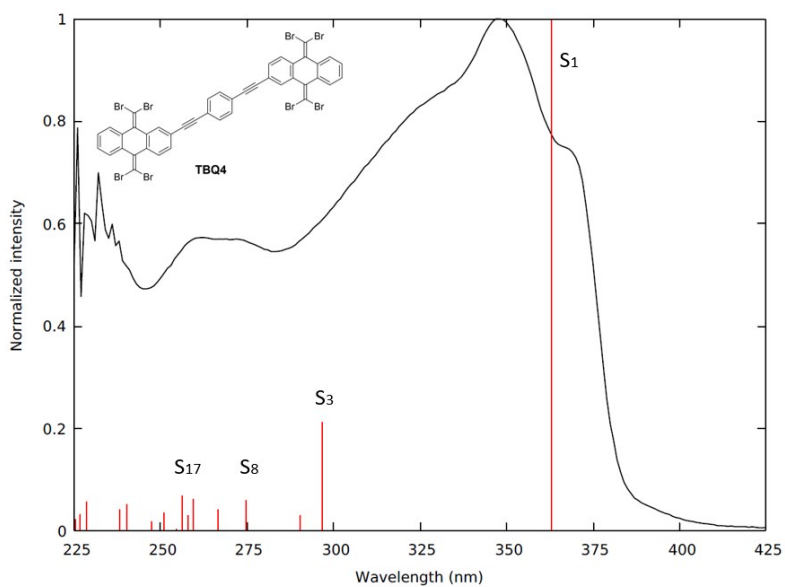


Figure S36. Experimental absorption spectra of **TBQ4** (black) and normalized oscillator strengths (red) of the calculated singlet excited (S_n) states.

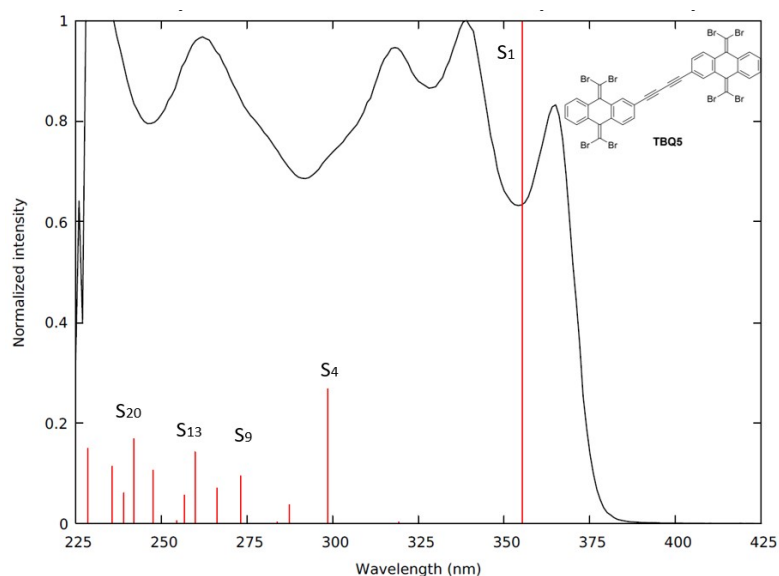


Figure S37. Experimental absorption spectra of **TBQ5** (black) and normalized oscillator strengths (red) of the calculated singlet excited (S_n) states.

Table S6. Description of the first two bright $S_0 \rightarrow S_n$ electronic transitions in terms of the molecular orbitals involved and the corresponding oscillator strengths for **TBQ1-5**.

TBQ1				TBQ2			
State	f	Monoexcitation	%	State	f	Monoexcitation	%
S_1	0.31	HOMO \rightarrow LUMO	63	S_1	1.71	HOMO \rightarrow LUMO	86
		HOMO-1 \rightarrow LUMO+1	25			HOMO-2 \rightarrow LUMO	14
		HOMO-5 \rightarrow LUMO+1	12	S_3	0.54	HOMO-1 \rightarrow LUMO+1	61
S_2	0.55	HOMO \rightarrow LUMO+1	43			HOMO-1 \rightarrow LUMO	39
		HOMO-1 \rightarrow LUMO	57	TBQ3			
State	f	Monoexcitation	%	State	f	Monoexcitation	%
S_1	1.59	HOMO \rightarrow LUMO	71	S_1	2.90	HOMO \rightarrow LUMO	84
		HOMO-1 \rightarrow LUMO+1	17			HOMO \rightarrow LUMO+2	16
		HOMO-5 \rightarrow LUMO+1	12	S_3	0.62	HOMO-1 \rightarrow LUMO+1	30
S_3	0.63	HOMO-3 \rightarrow LUMO	17			HOMO-2 \rightarrow LUMO	36
		HOMO-2 \rightarrow LUMO	29			HOMO-2 \rightarrow LUMO+2	12
HOMO-1 \rightarrow LUMO+1	36	TBQ4					
State	f	Monoexcitation	%	State	f	Monoexcitation	%
S_1	1.98	HOMO \rightarrow LUMO	67	S_4	0.53	HOMO-1 \rightarrow LUMO+1	11
		HOMO \rightarrow LUMO+2	11			HOMO-2 \rightarrow LUMO	53
		HOMO-2 \rightarrow LUMO	11			HOMO-5 \rightarrow LUMO	36

Table S7. Comparison of the wavelength calculated for the $S_0 \rightarrow S_1$ electronic transition with that of the experimental lowest-energy absorption band.

	$\lambda_{\text{abs,exp}}$ (nm)	$\lambda_{\text{theor}} (S_0 \rightarrow S_1)$ (nm)
TBQ1	300	302
TBQ2	349	336
TBQ3	314	313
TBQ4	368	363
TBQ5	365	355

S12. Natural transition orbitals involved in the $S_0 \rightarrow S_1$ excitation for TBQ1-5

The Natural Transition Orbitals (NTOs) for the S_1 excitation of **TBQ1–5** dimers are shown in Figures S38–S42, the contribution to the total excitation of each pair of NTOs detailed therein. For **TBQ1** and **TBQ3**, more than one NTO excitation is needed to describe the S_1 excitation more accurately compared to the rest of TBQ derivatives.

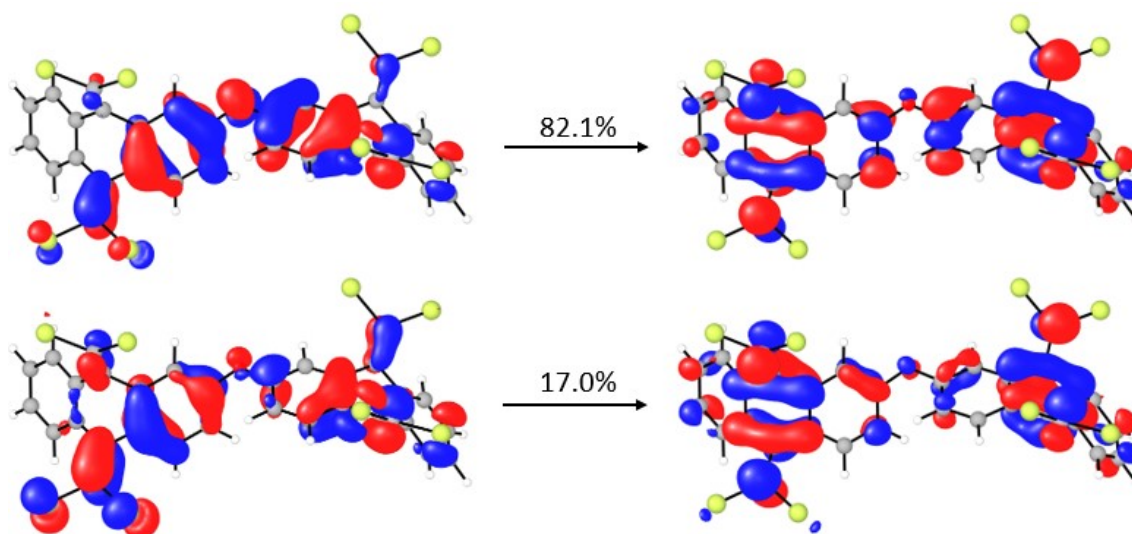


Figure S38. Natural Transition Orbitals for **TBQ1** and the contribution of each pair of NTOs to the S_1 excitation.

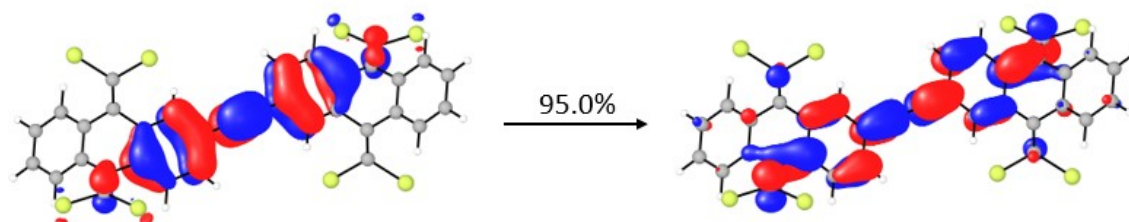


Figure S39. Natural Transition Orbitals for **TBQ2** and the contribution of the pair of NTOs to the S_1 excitation.

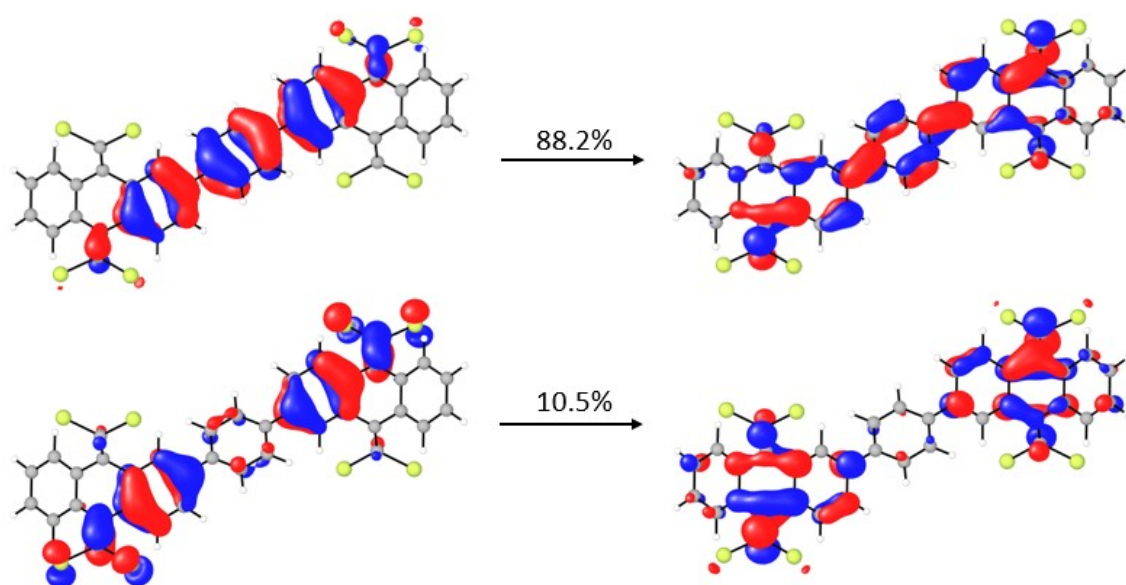


Figure S40. Natural Transition Orbitals for **TBQ3** and the contribution of each pair of NTOs to the S_1 excitation.

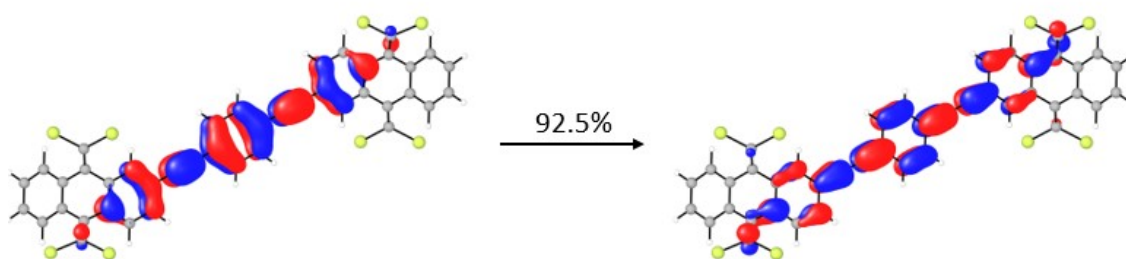


Figure S41. Natural Transition Orbitals for **TBQ4** and the contribution of the pair of NTOs to the S_1 excitation.

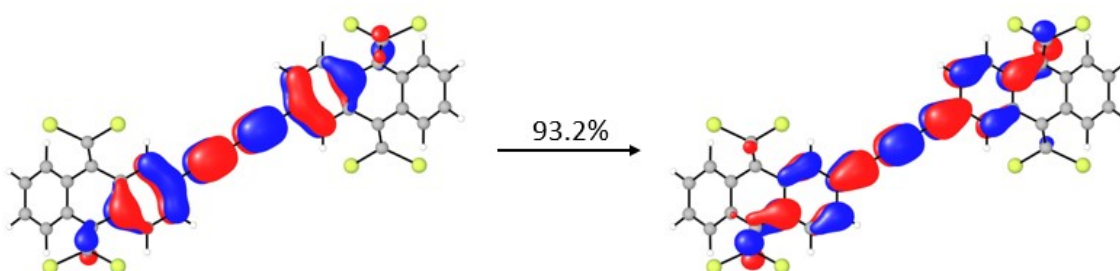


Figure S42. Natural Transition Orbitals for **TBQ5** and the contribution of the pair of NTOs to the S_1 excitation.

S13. Effect of TBAQ torsion on the absorption spectra

The theoretical $S_0 \rightarrow S_n$ transitions of **TBQ2**, **TBQ4** and **TBQ5** are calculated at the BMK/6-31G(d,p)+PCM level along the **TBAQ** torsion profile (Figure 3, S28 and S29, respectively) and compared with the experimental absorption spectra in Figures S43–S45.

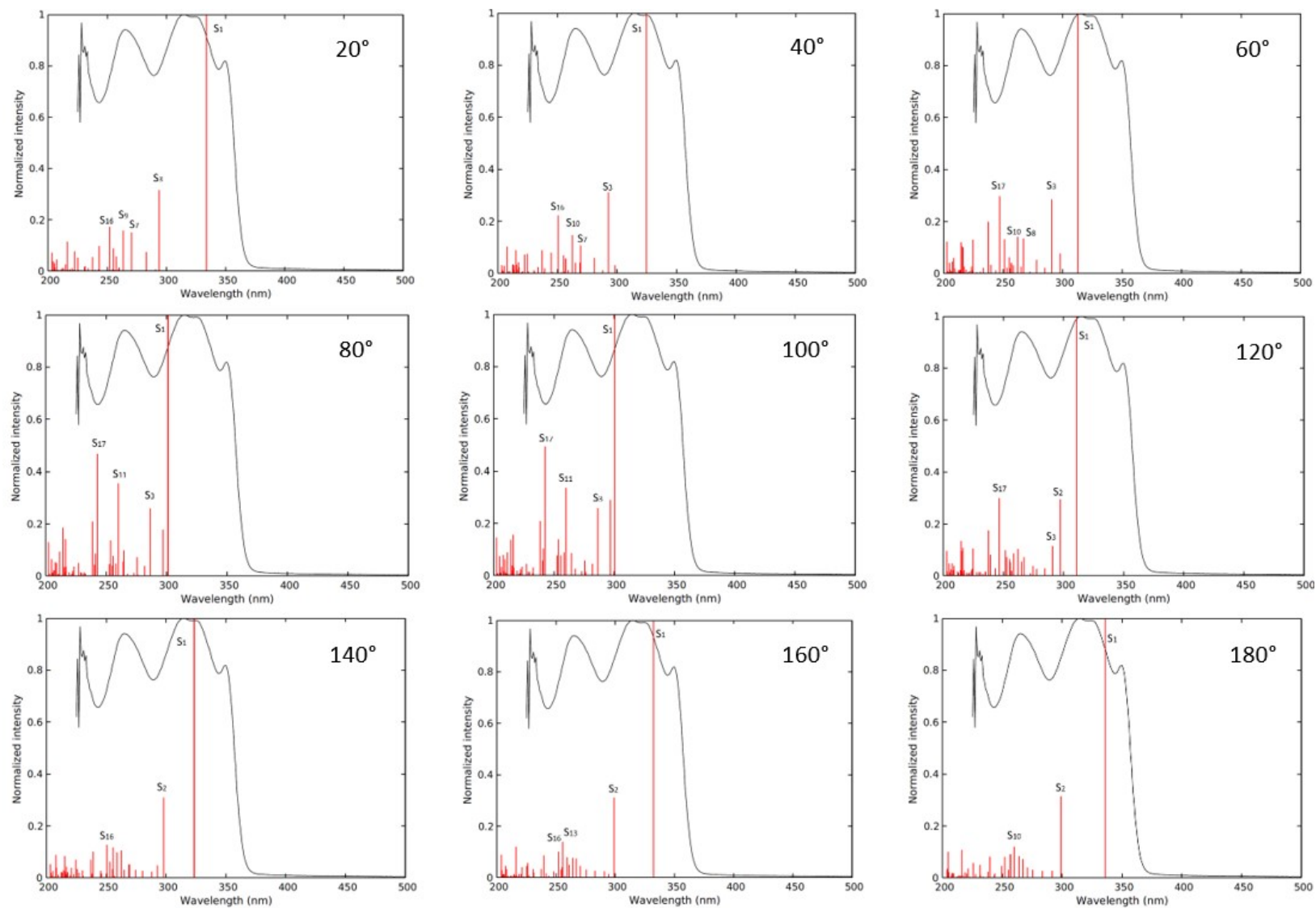


Figure S43. Experimental absorption spectra (black) and electronic transitions (red) along the torsion profile for **TBQ2**. For the spectrum of $\theta = 0^\circ$ dihedral angle, see Figure S34.

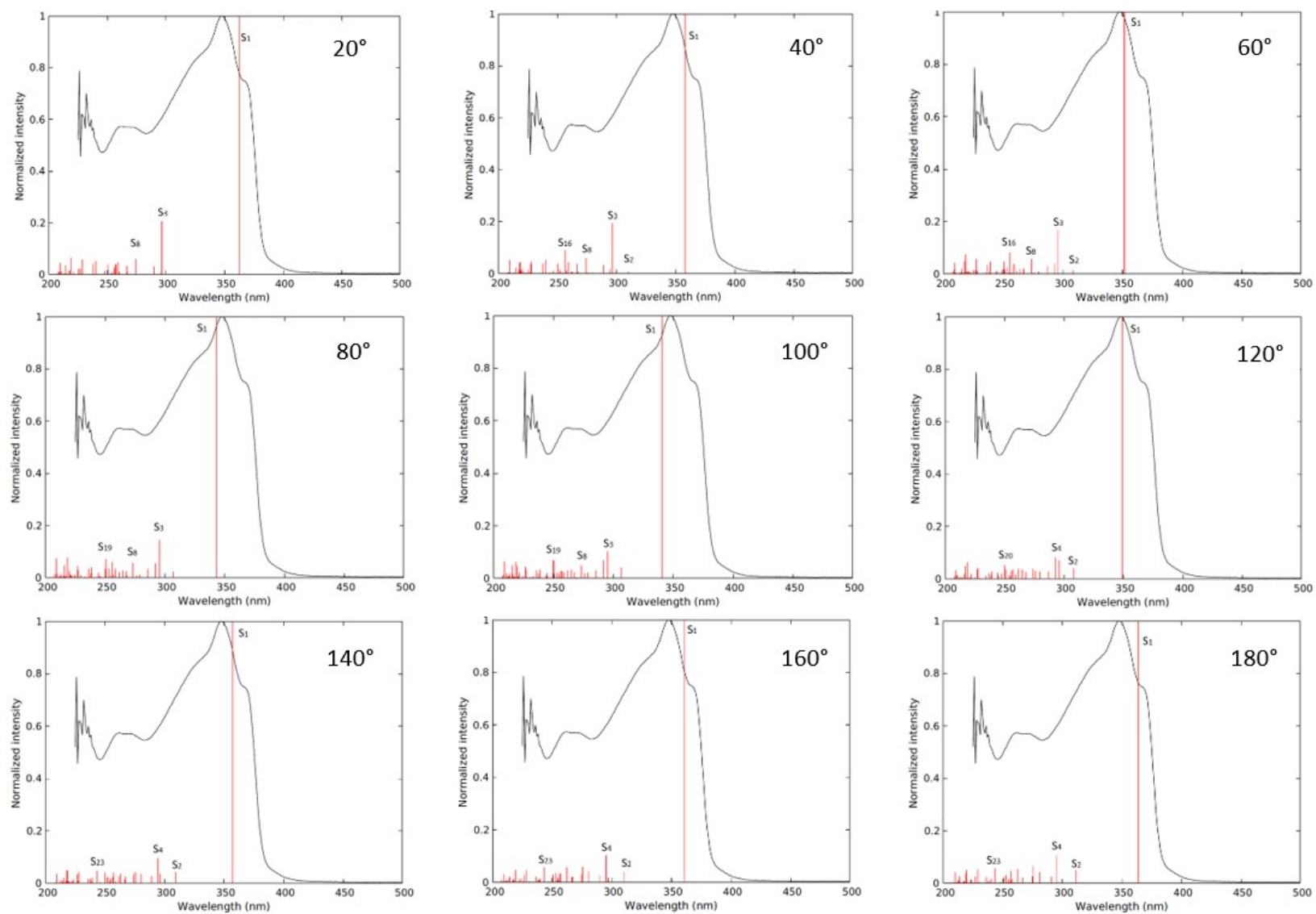


Figure S44. Experimental absorption spectra (black) and electronic transitions (red) along the torsion profile for **TBQ4**. For the spectrum of $\theta = 0^\circ$ dihedral angle, see Figure S36.

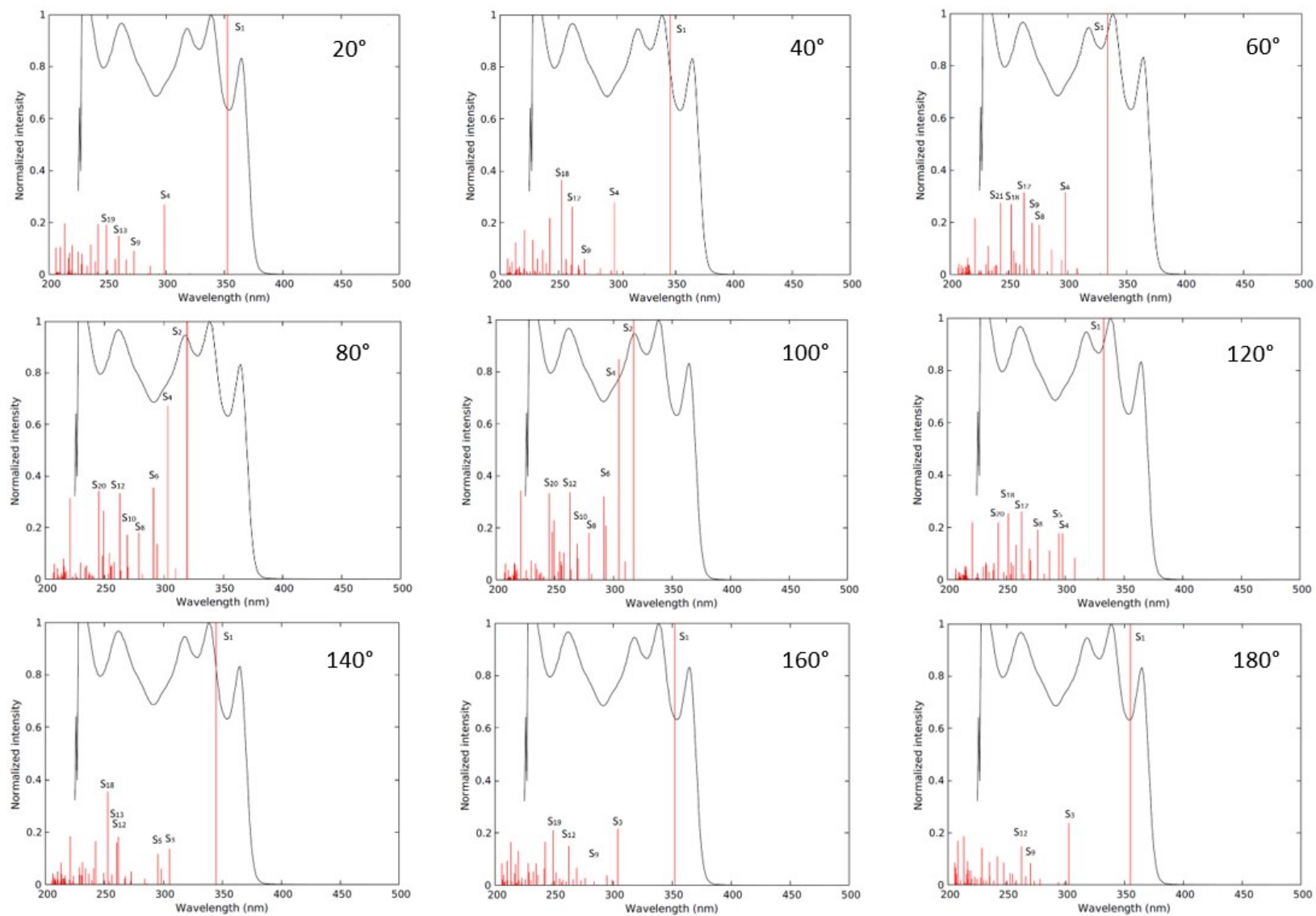


Figure S45. Experimental absorption spectra (black) and electronic transitions (red) along the torsion profile for **TBQ5**. For the spectrum of $\theta = 0^\circ$ dihedral angle, see Figure S37.

S14. DFT benchmark

To ensure a correct theoretical description of the **TBQ1-5** dimers, the molecular features of the **TBAQ** isomers were systematically investigated under a DFT framework. Our benchmark comprised calculations performed using BMK, M06-2X, ω B97X-D and B3LYP functionals with both 6-31G(d,p) and cc-pVTZ basis sets. The relative energies between the different isomers, shown in Figure 1, were assessed using both the electronic energy and its zero-point corrected value. The results are shown in Tables S8-S11 and from them can be concluded that the trends in the relative energy between the different conformations of **TBAQ** are preserved when using zero-point corrected electronic energies (the largest variations at the BMK/6-31G(d,p) level are 0.73 kcal/mol and 1.38 kcal/mol for the C_{2v} and C_{2h} minima, respectively) and that they are barely influenced by the choice of the DFT functional (the largest variation when using the 6-31G(d,p) basis set and going from BMK to M06-2X is 4.0 kcal/mol and 3.2 kcal/mol when going from BMK to ω B97X-D) and the basis set used (when the cc-pVTZ basis set is used, the largest variations are 3.13 kcal/mol for BMK, 1.57 kcal/mol for M06-2X and 2.59 kcal/mol for ω B97X-D). As a result, the 6-31G(d,p) basis set as selected for our calculations and we have used the electronic energy to evaluate the relative energy differences between **TBAQ** and **TCAQ** isomers and the rotational barriers for the **TBQ1-5** dimers.

Table S8. Relative electronic energy between the different conformations of **TBAQ** at the BMK/6-31G(d,p) and BMK/cc-pVTZ levels of theory. Zero-point corrected values are shown between parentheses.

Conformation	Relative electronic energy (kcal mol ⁻¹)	
	6-31G(d,p)	cc-pVTZ
D_{2h}	0.00 (0.00)	0.00 (0.00)
D_2	-19.81 (-19.20)	-20.22 (-19.37)
C'_{2h}	-20.48 (-20.31)	-20.52 (-20.99)
C^*_{2h}	-20.48 (-20.31)	-20.52 (-20.99)
C_{2h}	-31.28 (-29.90)	-32.51 (-30.93)
C_{2v}	-53.80 (-53.07)	-56.92 (-58.00)

Table S9. Relative electronic energy between the different conformations of **TBAQ** at the ω B97X-D/6-31G(d,p) and ω B97X-D/cc-pVTZ levels of theory. Zero-point corrected values are shown between parentheses.

Conformation	Relative electronic energy (kcal mol ⁻¹)	
	6-31G(d,p)	cc-pVTZ
D_{2h}	0.00 (0.00)	0.00 (0.00)
D_2	-19.81 (-19.63)	-20.10 (-20.08)
C'_{2h}	-20.69 (-20.18)	-20.68 (-20.62)
C^*_{2h}	-20.69 (-20.18)	-20.68 (-20.62)
C_{2h}	-33.58 (-33.34)	-34.28 (-34.27)
C_{2v}	-56.97 (-57.20)	-59.55 (-59.40)

Table S10. Relative electronic energy between the different conformations of **TBAQ** at the M06-2X/6-31G(d,p) and M06-2X/cc-pVTZ levels of theory. Zero-point corrected values are shown between parentheses.

Conformation	Relative electronic energy (kcal mol ⁻¹)	
	6-31G(d,p)	cc-pVTZ
<i>D</i> _{2h}	0.00 (0.00)	0.00 (0.00)
<i>D</i> ₂	-22.36 (-21.88)	-22.07 (-21.71)
<i>C'</i> _{2h}	-23.36 (-22.80)	-22.82 (-22.47)
<i>C*</i> _{2h}	-23.26 (-22.80)	-22.82 (-20.47)
<i>C</i> _{2h}	-35.79 (-35.16)	-35.97 (-30.93)
<i>C</i> _{2v}	-58.11 (-57.59)	-59.69 (-59.24)

Table S11. Relative electronic energy between the different conformations of **TBAQ** at the B3LYP/6-31G(d,p) and B3LYP/cc-pVTZ levels of theory. Zero-point corrected values are shown between parentheses.

Conformation	Relative electronic energy (kcal mol ⁻¹)	
	6-31G(d,p)	cc-pVTZ
<i>D</i> _{2h}	0.00 (0.00)	0 (0.00)
<i>D</i> ₂	-18.74 (-18.62)	-19.40 (-19.35)
<i>C'</i> _{2h}	-19.33 (-19.08)	-19.62 (-19.59)
<i>C*</i> _{2h}	-19.33 (-19.08)	-19.62 (-19.59)
<i>C</i> _{2h}	-28.48 (-28.09)	-29.26 (-29.02)
<i>C</i> _{2v}	-50.48 (-50.17)	-53.18 (-52.95)

The selection of the BMK functional for the description of the structural, electronic and optical properties of **TBQ1–5** was motivated by accurate description of the absorption spectra, especially when **TBAQ**-to-**TBAQ** rotations are considered (see Section S13). The BMK/6-31G(d,p)+PCM(CH₂Cl₂) results are more accurate compared to those obtained at the B3LYP/6-31G(d,p) (CH₂Cl₂) level, due to the over-delocalization of the FMOs involved in the S₀→S₁ excitation, as it can be seen in Figure S46. The character of the excitation, mostly HOMO–LUMO for all dimers, is listed in Table S12 and results in a significant red-shift compared to the experimental spectra and the BMK-based results (see Table S7). The nature of the HOMO and LUMO is very similar for both functionals but the energy difference between them is smaller for B3LYP due to the destabilization of the HOMO and the stabilization of the LUMO (Table S13). Regarding the rest of the properties that were benchmarked and compared, the relative energies of the different conformations for both **TCAQ** and **TBAQ** (listed in Table S14) are very similar to those computed with the BMK functional.

Table S12. Excitation energy (E , in eV and nm), oscillator strength (f) and description in terms of molecular orbitals calculated at the B3LYP/6-31G(d,p)+PCM(CH₂Cl₂) level of theory for the $S_0 \rightarrow S_1$ electronic transition of **TBQ1–5**, compared to the experimental absorption wavelength.

	E (eV)	λ (nm)	f	Monoexcitation	%	λ_{exp} (nm)
TBQ1	3.61	343	0.22	HOMO \rightarrow LUMO HOMO-2 \rightarrow LUMO	83 17	300
TBQ2	3.25	381	1.37	HOMO \rightarrow LUMO	100	349
TBQ3	3.46	358	1.06	HOMO \rightarrow LUMO HOMO-2 \rightarrow LUMO	85 15	314
TBQ4	2.96	419	2.47	HOMO \rightarrow LUMO	100	368
TBQ5	3.06	405	1.78	HOMO \rightarrow LUMO	100	365

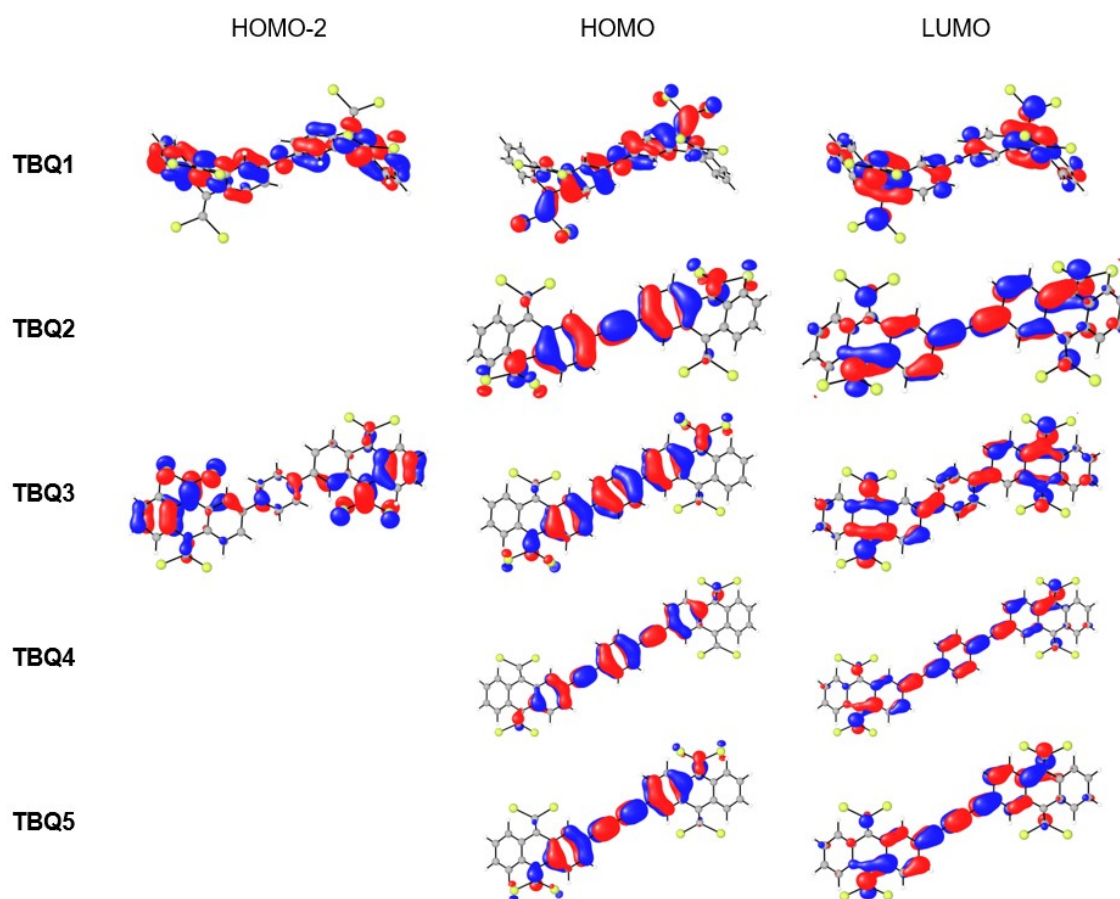


Figure S46. Frontier molecular orbitals calculated for **TBQ1–5** at the B3LYP/6-31G(d,p)+PCM(CH₂Cl₂) level of theory that are involved in the $S_0 \rightarrow S_1$ excitation.

Table S13. HOMO and LUMO energies, and HOMO-LUMO energy gap calculated at the B3LYP/6-31G(d,p)+PCM(CH₂Cl₂) level for **TCAQ**, **TBAQ** and **TBQ1-5**.

	HOMO energy (eV)	LUMO energy (eV)	H-L energy gap (eV)
TCAQ	-7.06	-3.55	3.51
TBAQ	-6.19	-1.84	4.35
TBQ1	-6.01	-1.93	4.08
TBQ2	-5.90	-2.23	3.67
TBQ3	-5.92	-2.01	3.89
TBQ4	-5.67	-2.30	3.37
TBQ5	-5.87	-2.37	3.50

Table S14. Relative energies (kcal mol⁻¹) of the different stationary structures calculated for **TBAQ** and **TCAQ** at the B3LYP/6-31G(d,p) and BMK/6-31G(d,p) level of theory in gas phase.

Conformation	TBAQ		TCAQ	
	BMK	B3LYP	BMK	B3LYP
<i>D</i> _{2h}	0.00	0.00	0.00	0.00
<i>C</i> _{2h}	-19.81	-19.34	-2.48	-2.50
<i>D</i> ₂	-20.48	-19.33	-3.90	-3.67
<i>C</i> _{2h}	-31.28	-18.74	-10.69	-9.16
<i>C</i> _{2v}	-53.80	-50.48	-22.28	-20.10

S15. Raman and IR experimental and calculated spectra

General details. Raman spectra were recorded in solid state in resonance conditions with the excitation wavelength at 785 nm. The measurements were carried out in the 1×1 camera of a Bruker Senterra Raman microscope (Nd:YAG laser at different wavelengths: 532, 633 and 785 nm) by averaging the spectra during 50 min with a resolution of 3–5 cm^{-1} . A CCD (Charge Couple Device) camera operating at $-50\text{ }^{\circ}\text{C}$ was used for detection.

The IR absorption studies have been performed in solid state (pellets obtained by diluting the sample in KBr) (KBr:Sigma-Aldrich/Merck, FT-IR grade, $\geq 99\%$) through a Bruker Tensor 27 FT-IR with a wavenumber range of 7500–370 cm^{-1} . The most widely employed IR spectrometer is that implementing the Fourier Transform technique (FT-IR). Instead of a dispersing element, the FT-IR spectrometers use a Michelson interferometer to produce an interferogram, which is then transformed in the IR spectrum through a Fourier Transform mathematical treatment.

As described above in Section S5, IR and Raman spectra were calculated at the BMK/6-31G(d,p) level of theory in gas phase. The vibrational frequencies were rescaled with a factor of 0.961.

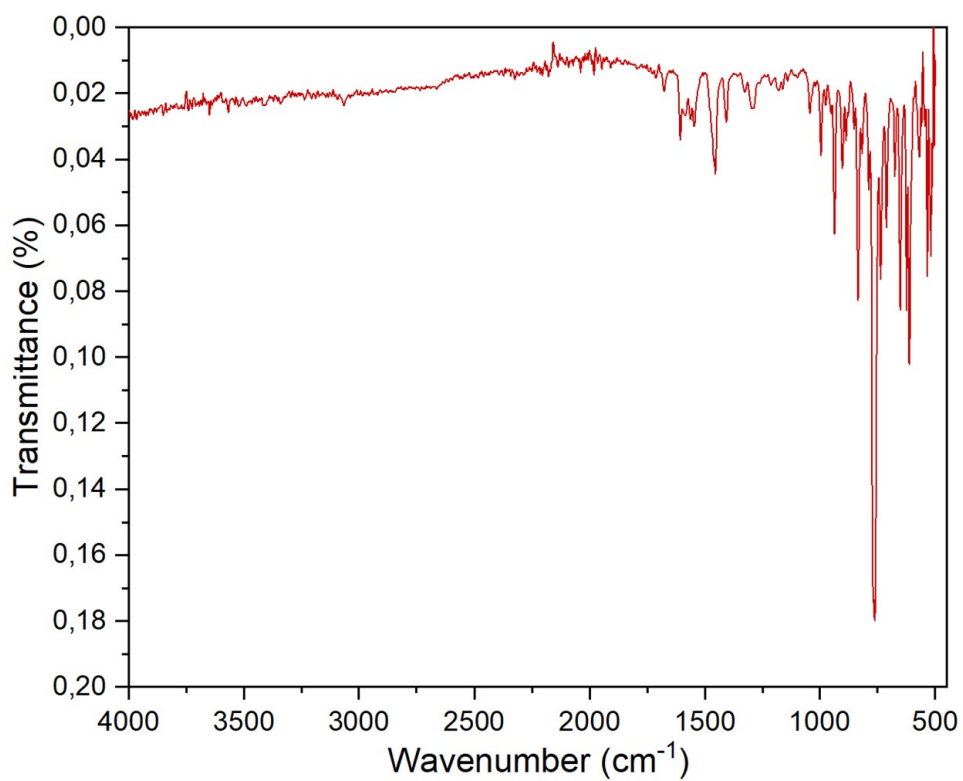


Figure S47. FTIR spectrum of TBQ2.

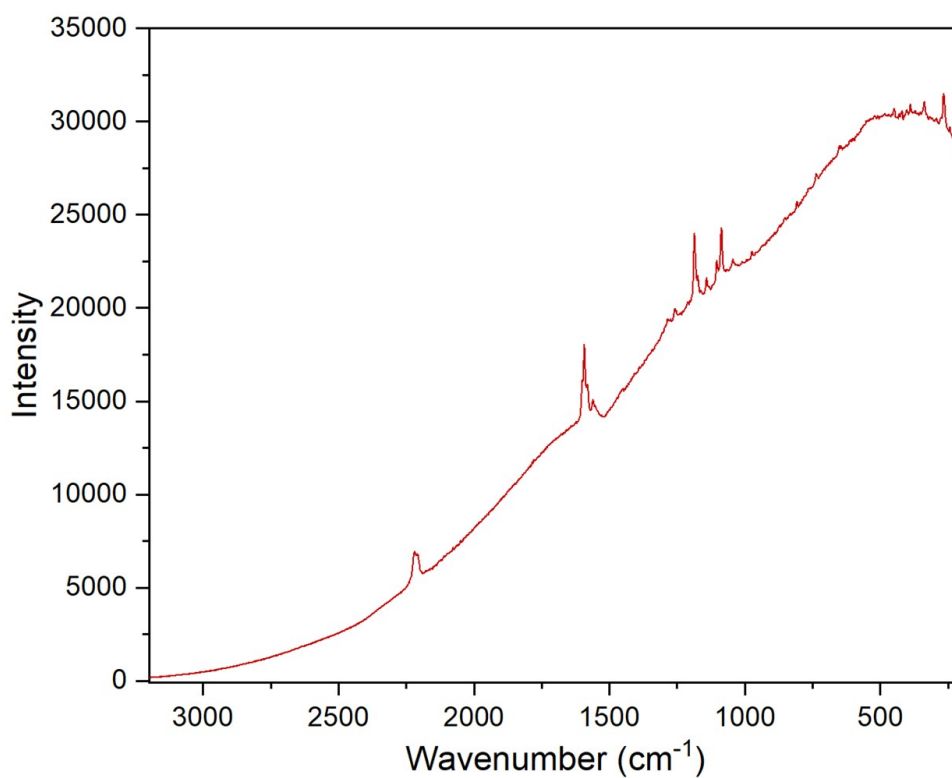


Figure S48. Raman spectrum of TBQ2.

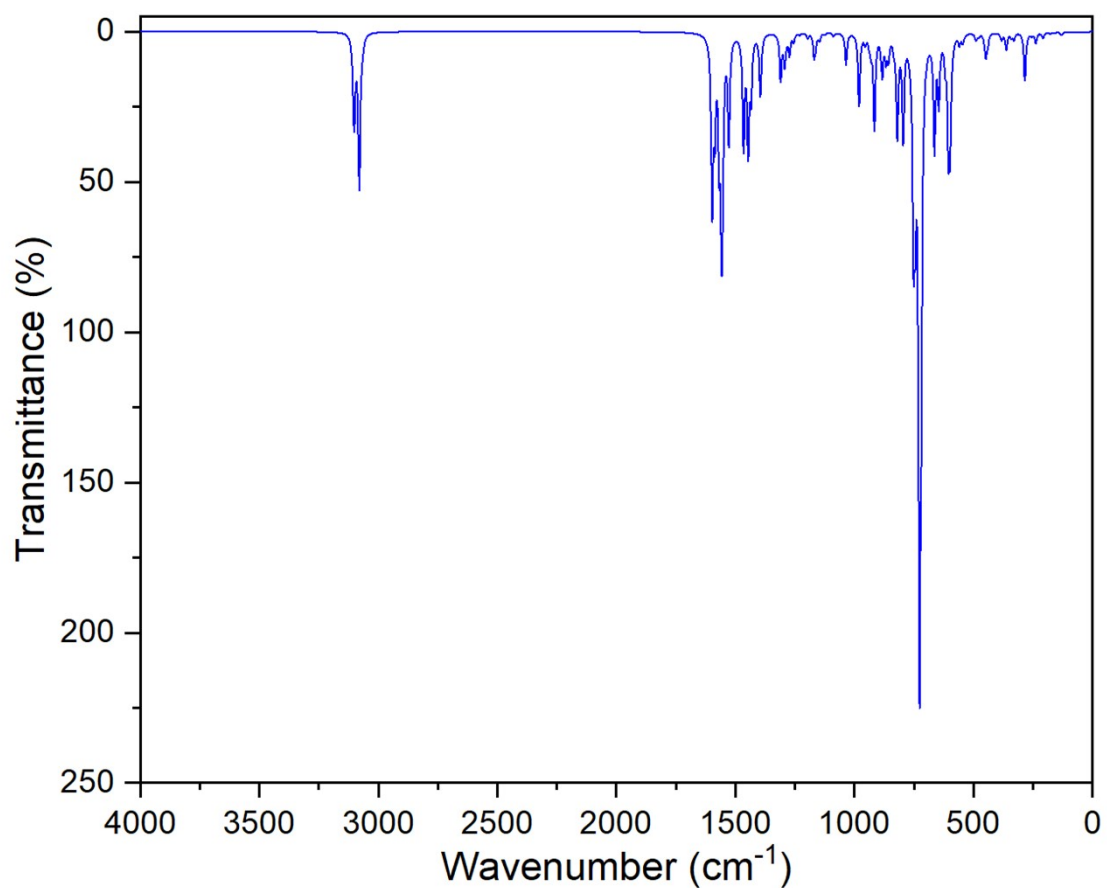


Figure S49. BMK/6-31G(d,p) simulated IR spectrum of TBQ2.

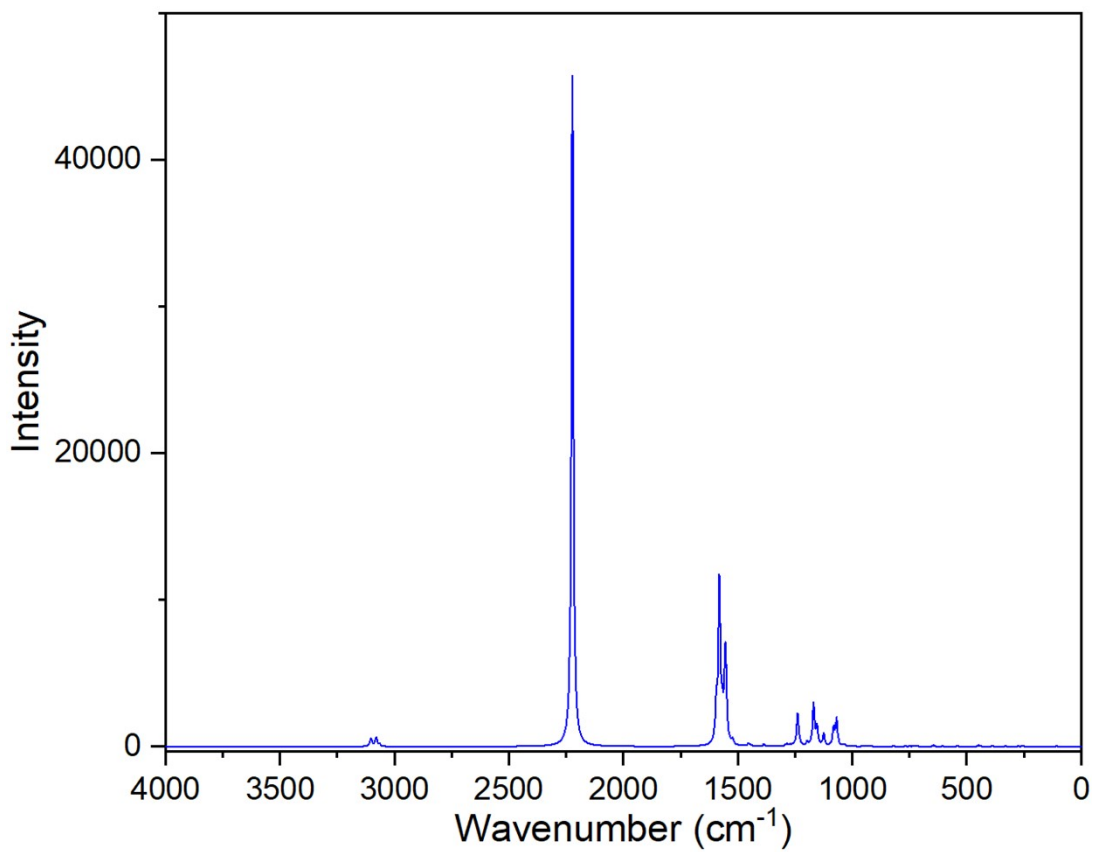


Figure S50. BMK/6-31G(d,p) simulated Raman spectrum of TBQ2.



Figure S51. FTIR spectrum of **TBQ3**.

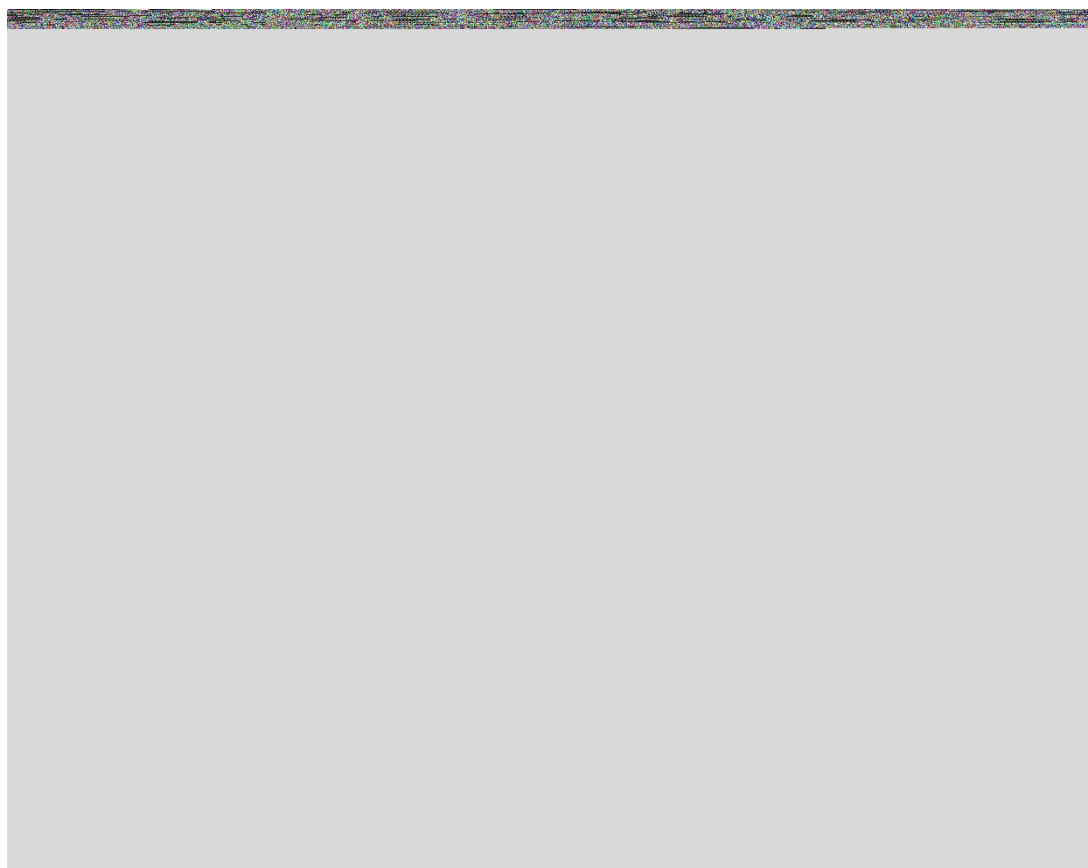


Figure S52. Raman spectrum of **TBQ3**.



Figure S53. BMK/6-31G(d,p) simulated IR spectrum of **TBQ3**.

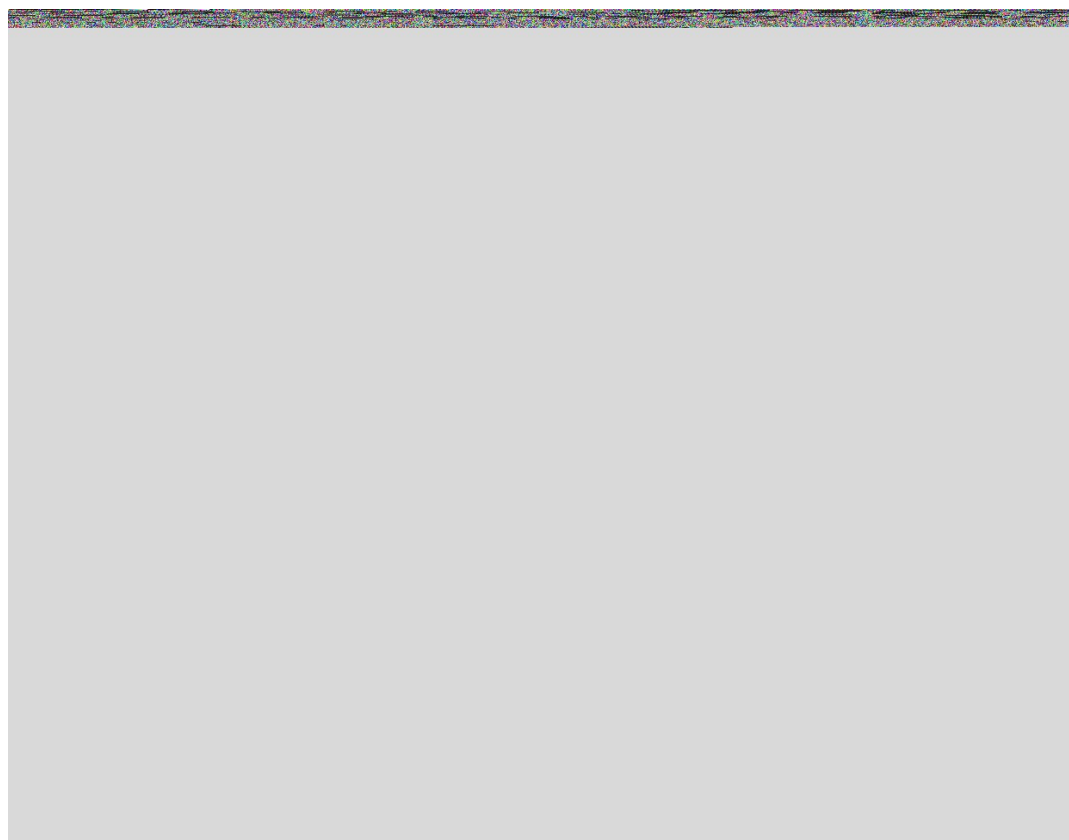


Figure S54. BMK/6-31G(d,p) simulated Raman spectrum of **TBQ3**.

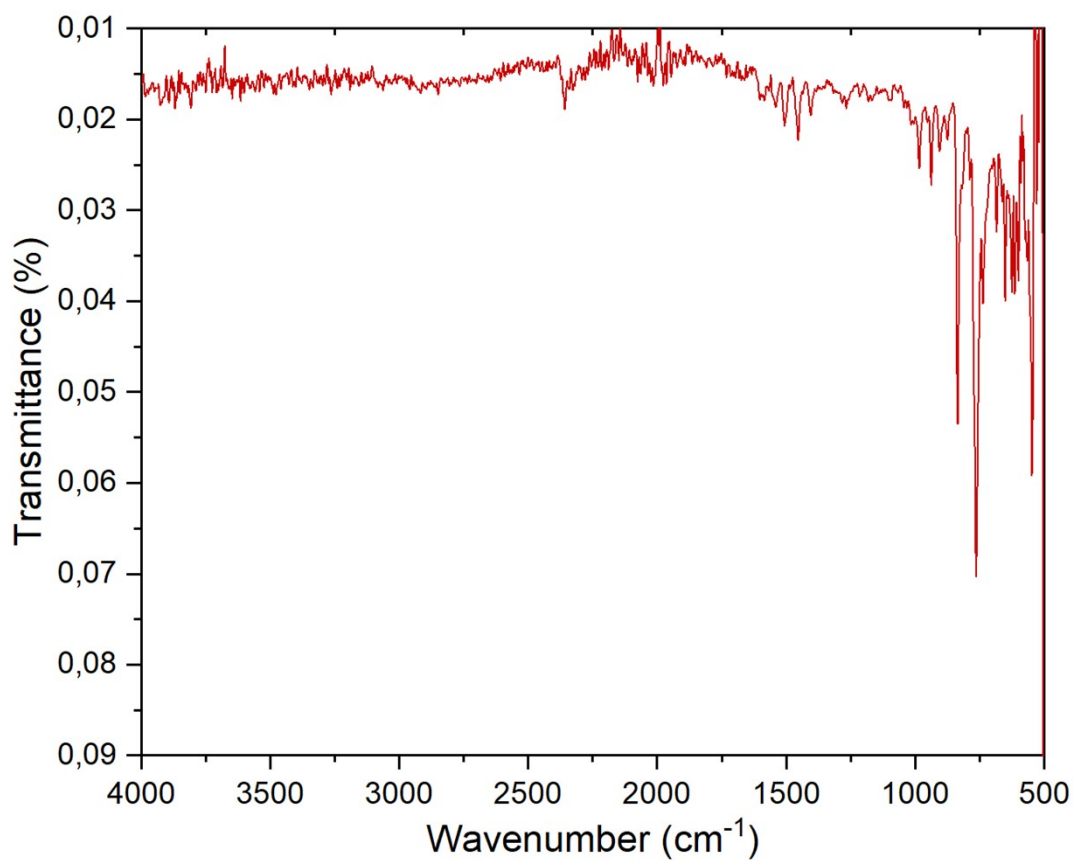


Figure S55. IR spectrum of TBQ4.

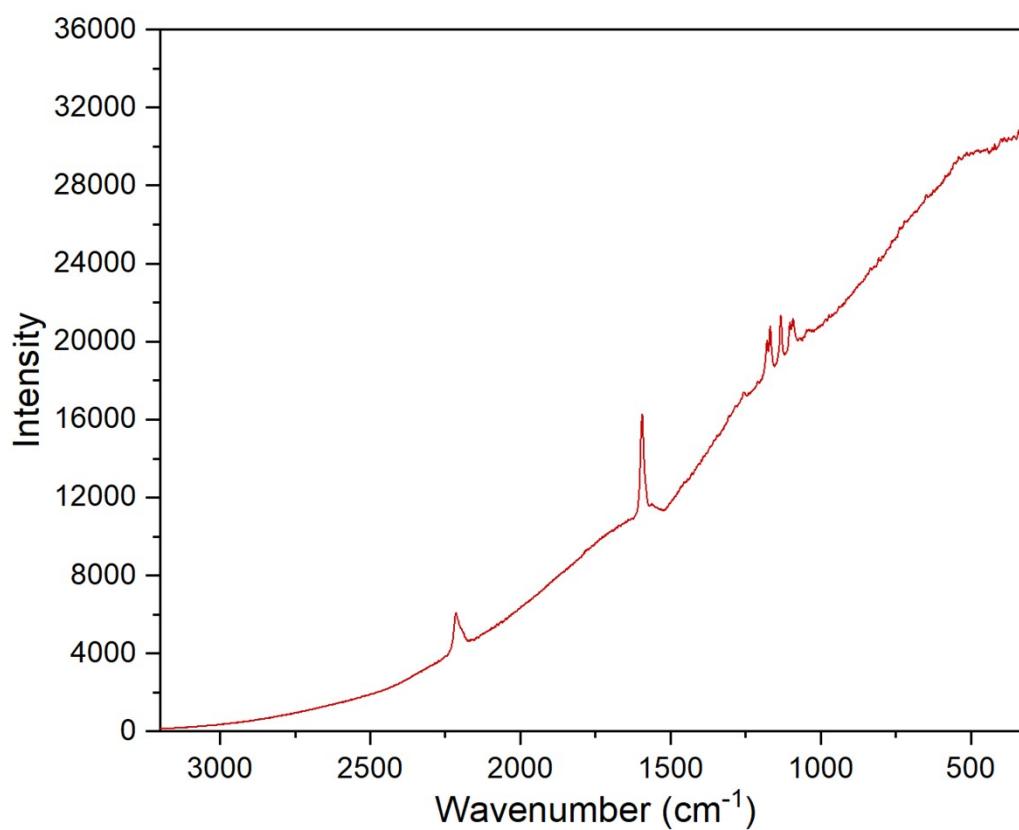


Figure S56. Raman spectrum of TBQ4.

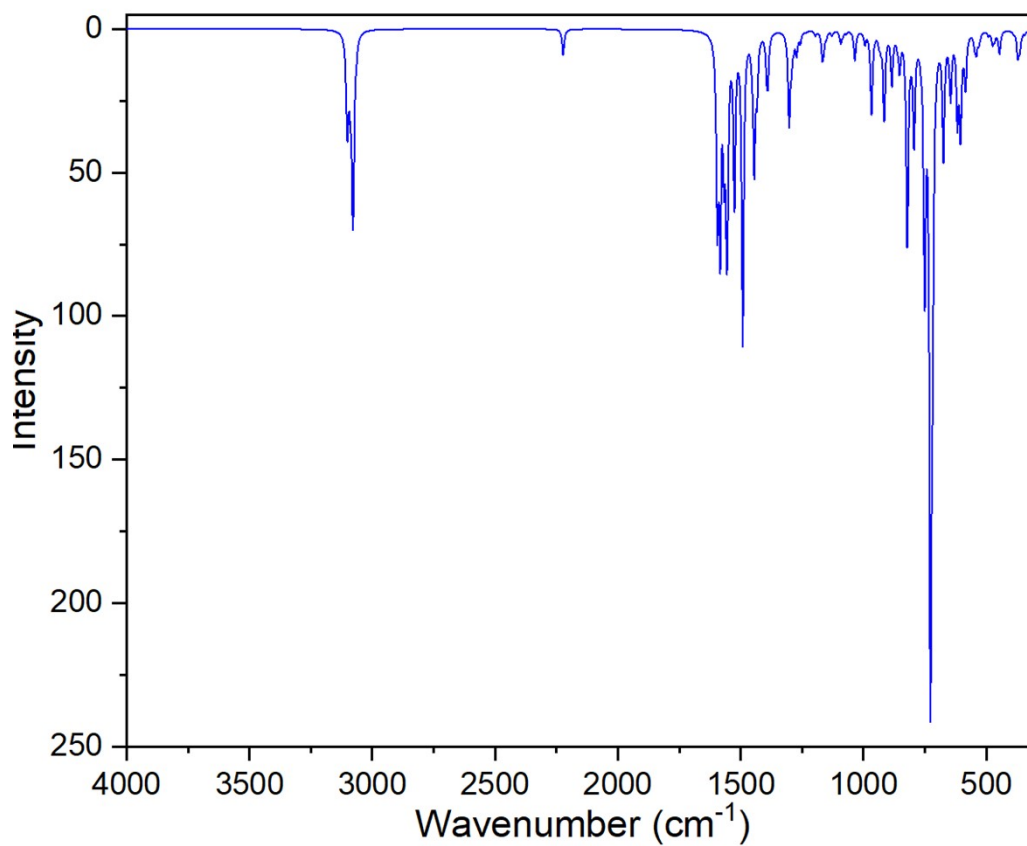


Figure S57. BMK/6-31G(d,p) simulated IR spectrum of TBQ4.

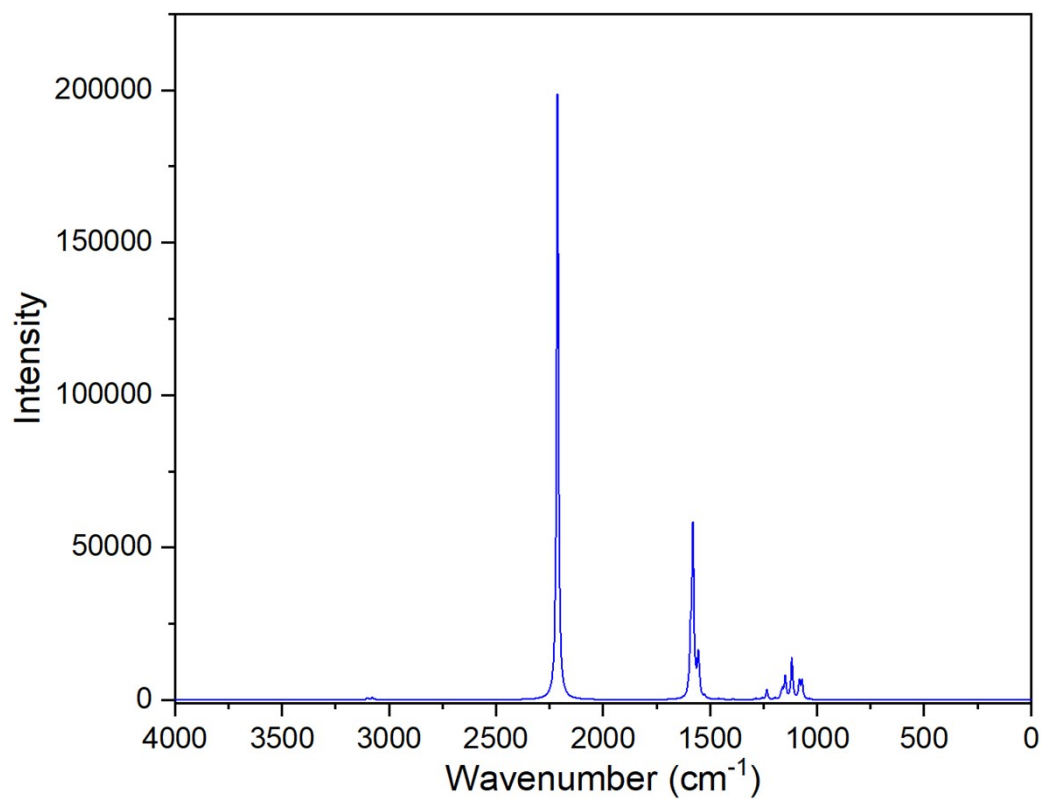


Figure S58. BMK/6-31G(d,p) simulated Raman spectrum of TBQ4.

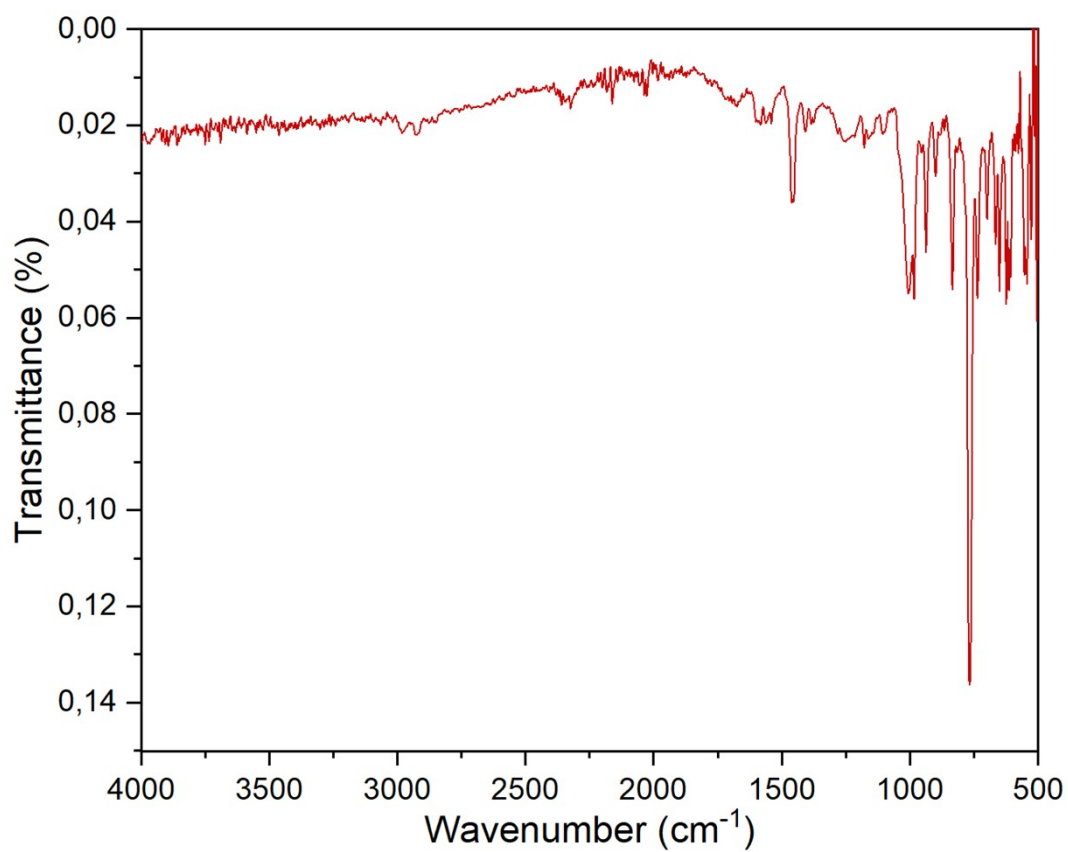


Figure S59. IR spectrum of TBQ5.

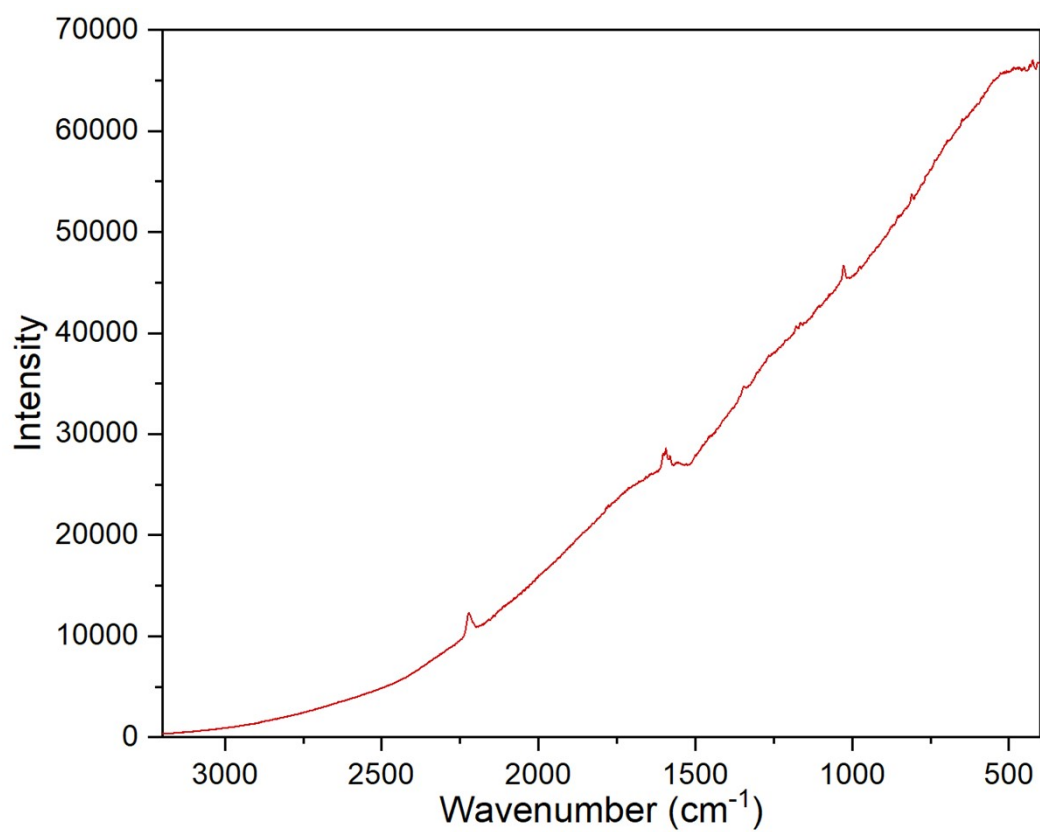


Figure S60. Raman spectrum of TBQ5.

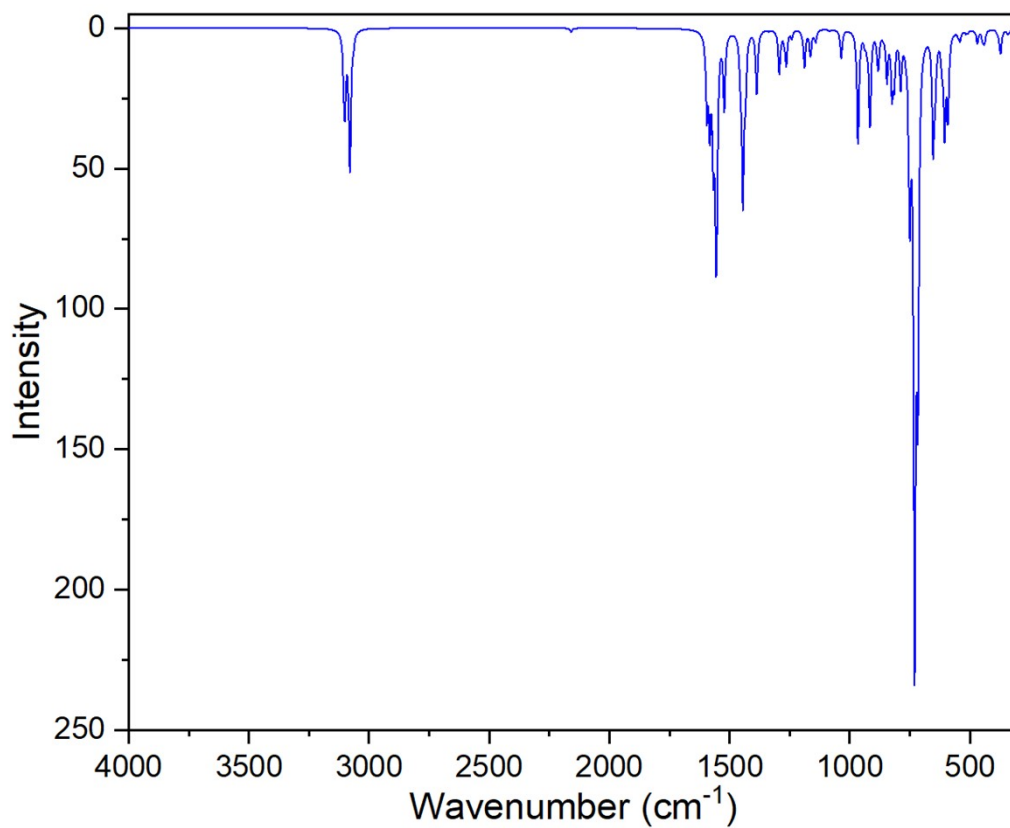


Figure S61. BMK/6-31G(d,p) simulated IR spectrum of TBQ5.

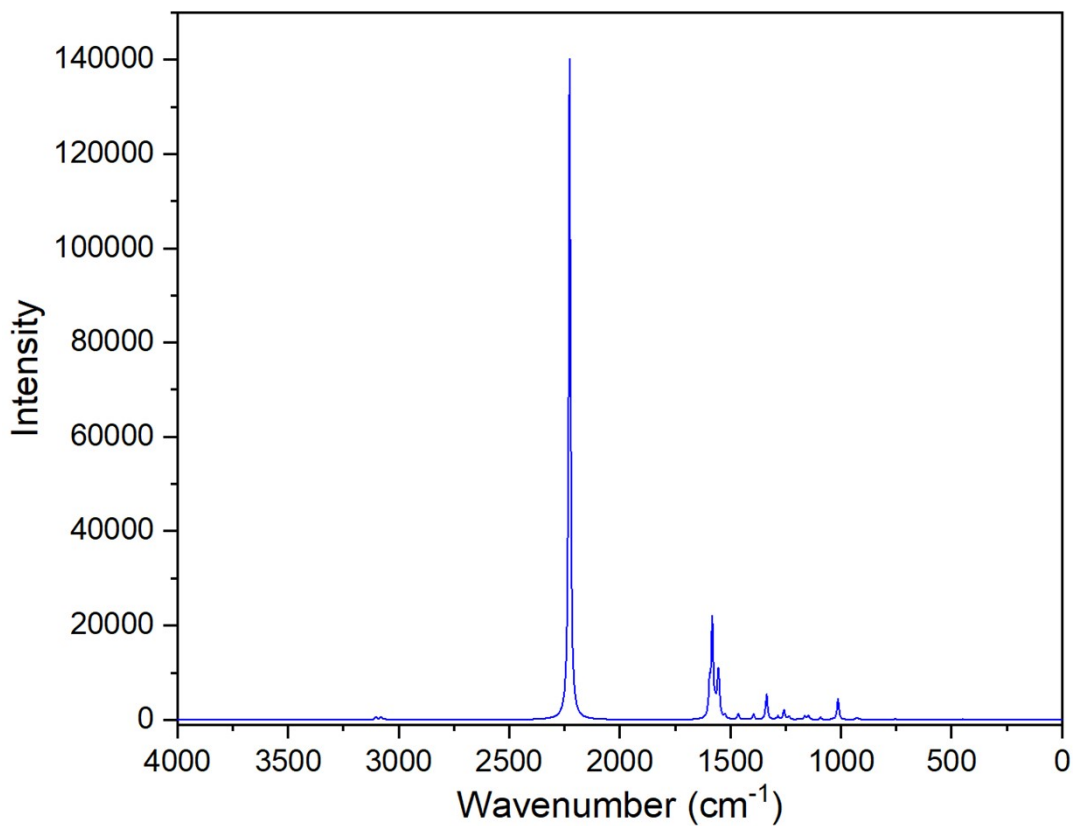


Figure S62. BMK/6-31G(d,p) simulated Raman spectrum of TBQ5.

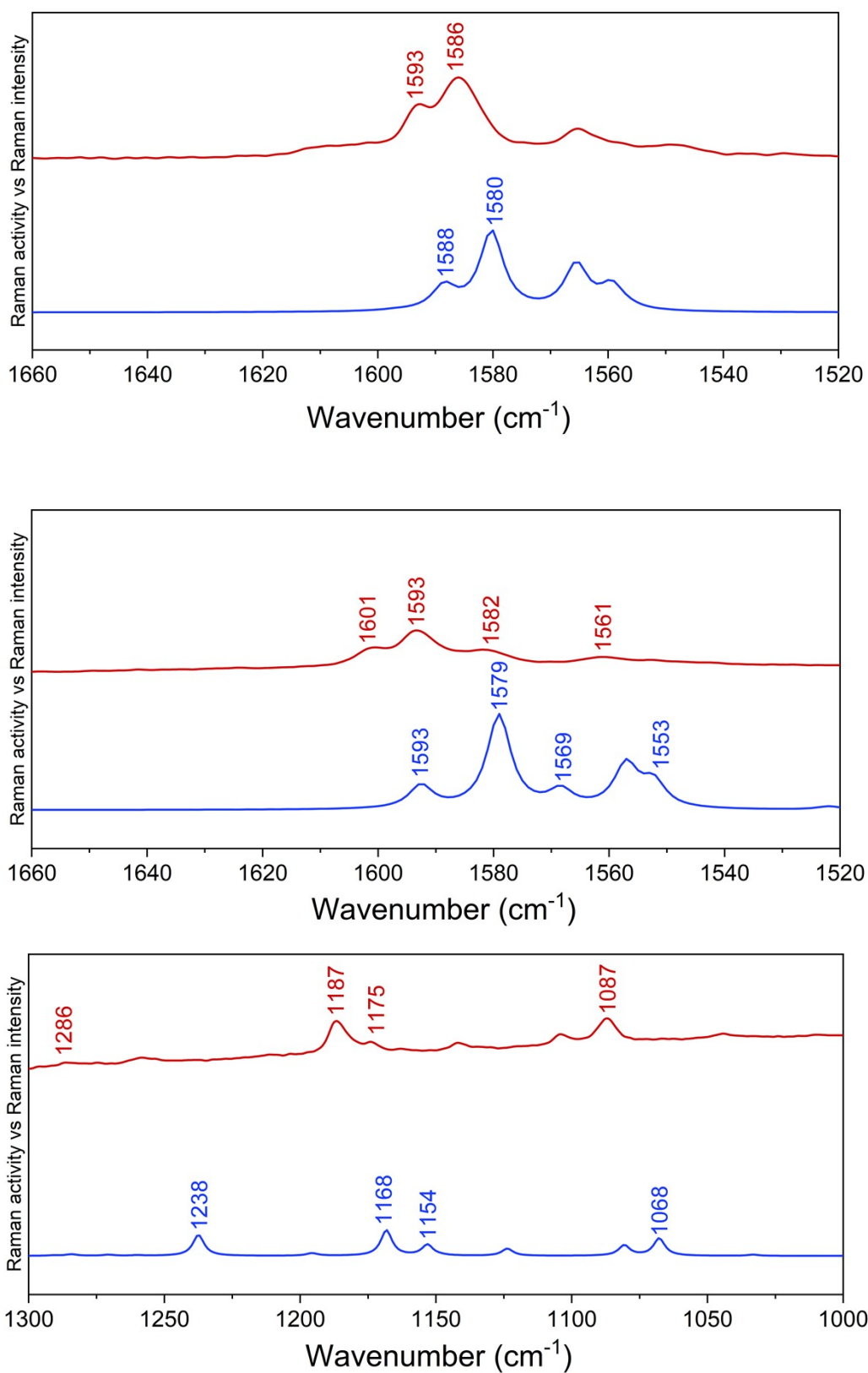


Figure S63. Compared BMK/6-31G(d,p) simulated (blue) and experimental (red) Raman spectra of **TBAQ** (above) and **TBQ2** at high energy (center) and low energy (below).

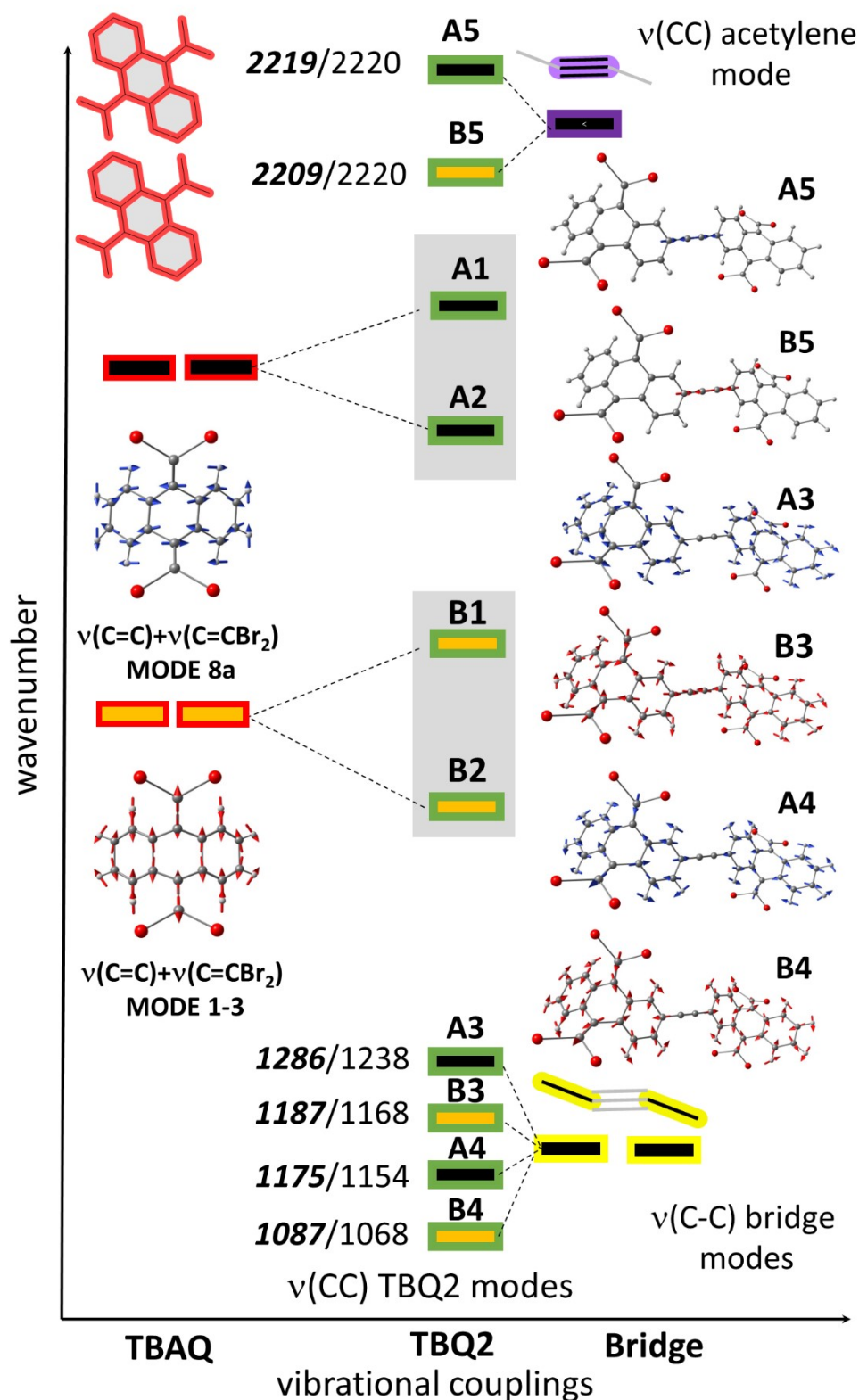


Figure S64. Wavenumber evolution of the $\nu(\text{CC})$ vibrational modes from the TBAQ units (in red) upon vibrational coupling with the central $\nu(\text{CC})$ acetylene spacer (in purple) and with the $\nu(\text{CC})$ of the single connecting bonds (in yellow). Vibrational normal modes are shown. Blue and red vectors indicate vibrational modes 1,3 and 8a of benzene rings, respectively. BMK/6-31G(d,p) theoretical wavenumbers (in cm^{-1}) are compared to the experimental values shown in bold.

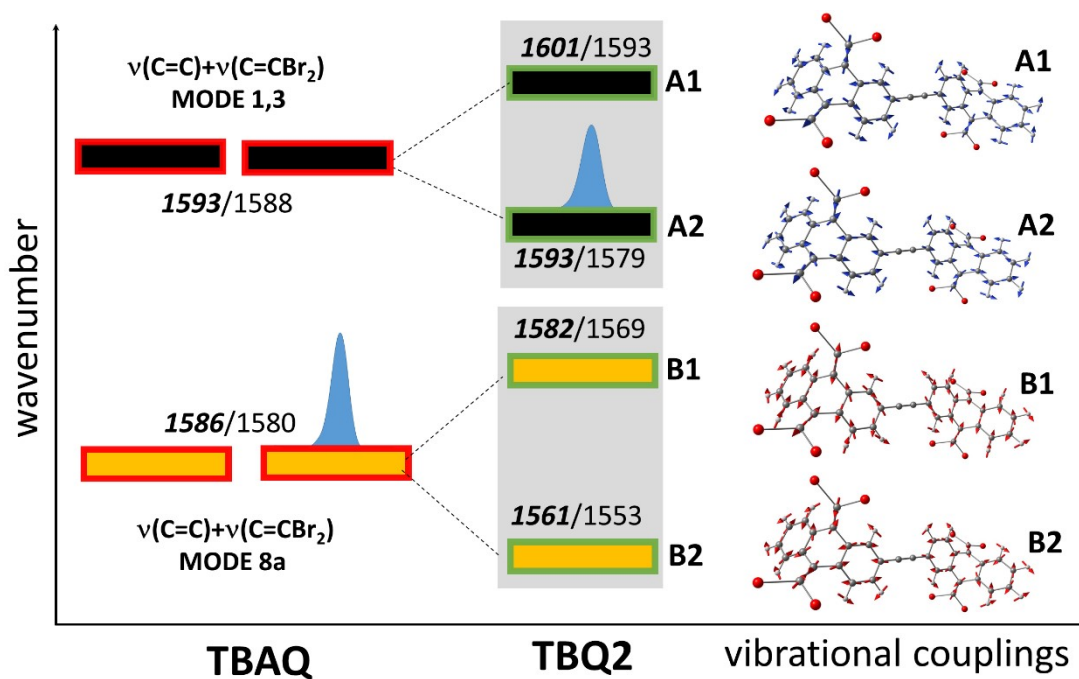


Figure S65. Wavenumber evolution of the $\nu(\text{CC})$ vibrational modes from the TBAQ units (in red) at high energy. Blue and red vectors indicate vibrational modes 1,3 and 8a of benzene rings, respectively. BMK/6-31G(d,p) theoretical wavenumbers (in cm^{-1}) are compared to the experimental values shown in bold font.

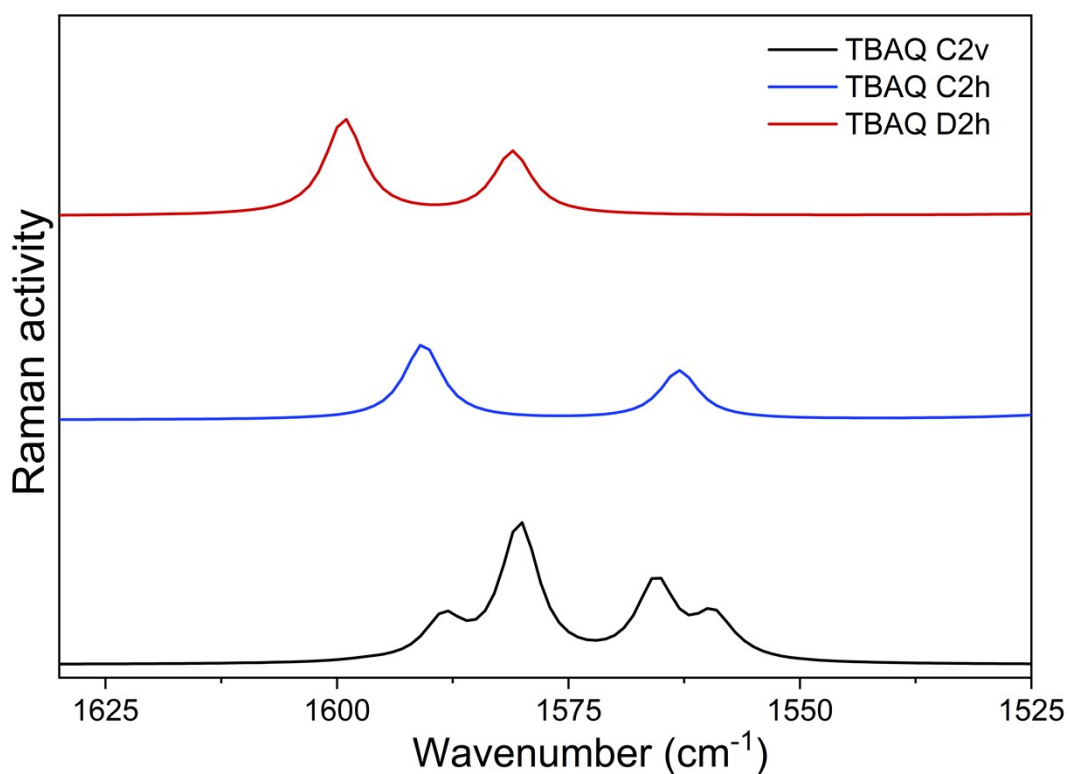


Figure S66. BMK/6-31G(d,p) theoretical Raman spectra of TBAQ calculated at the C_{2v} , C_{2h} and D_{2h} optimized geometries.

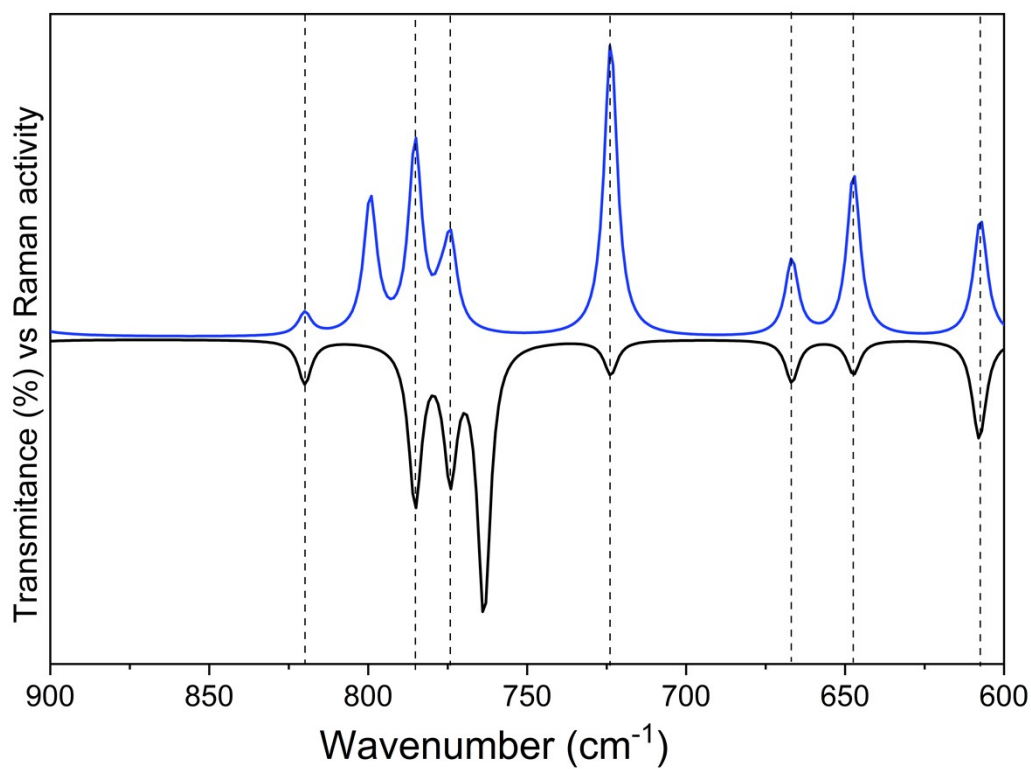
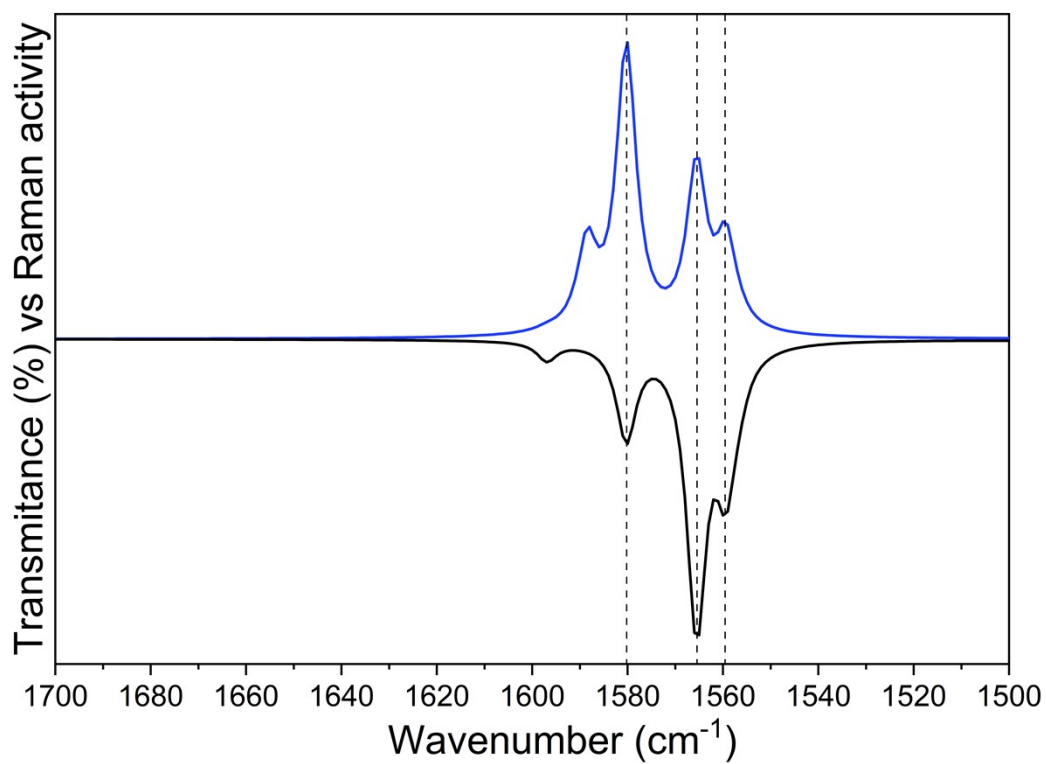


Figure S67. Comparison between theoretical Raman (blue line) and IR (black line) spectra at high (above) and low (below) energy of **TBAQ**. Bands are normalized to the strongest Raman and infrared bands.

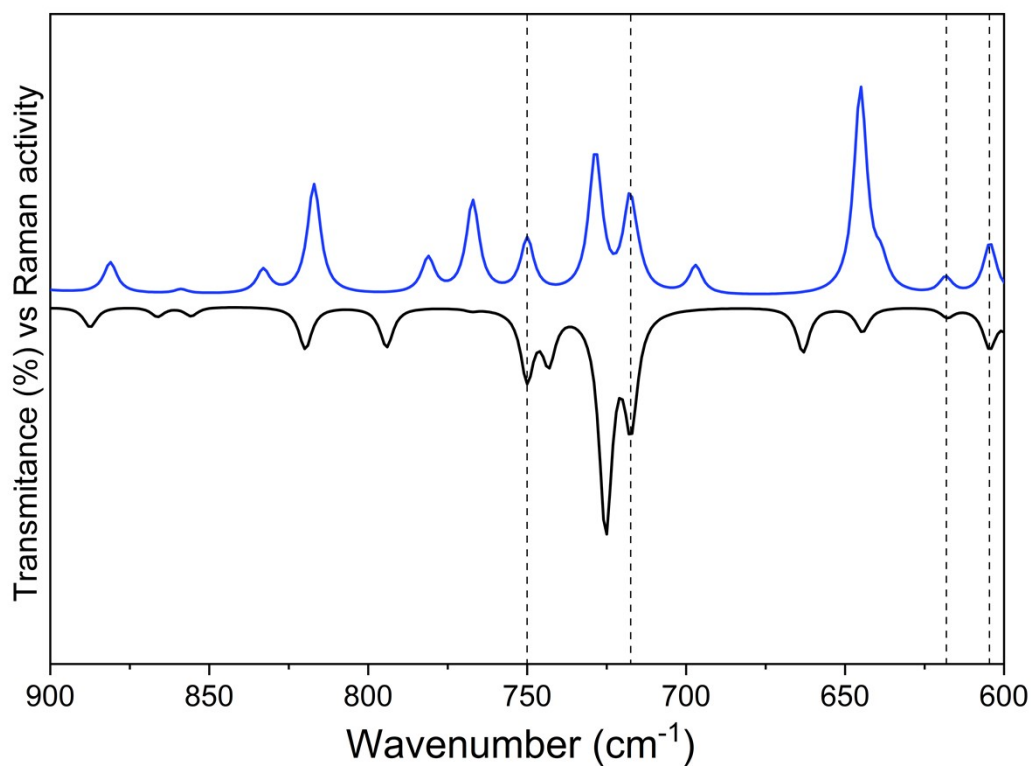
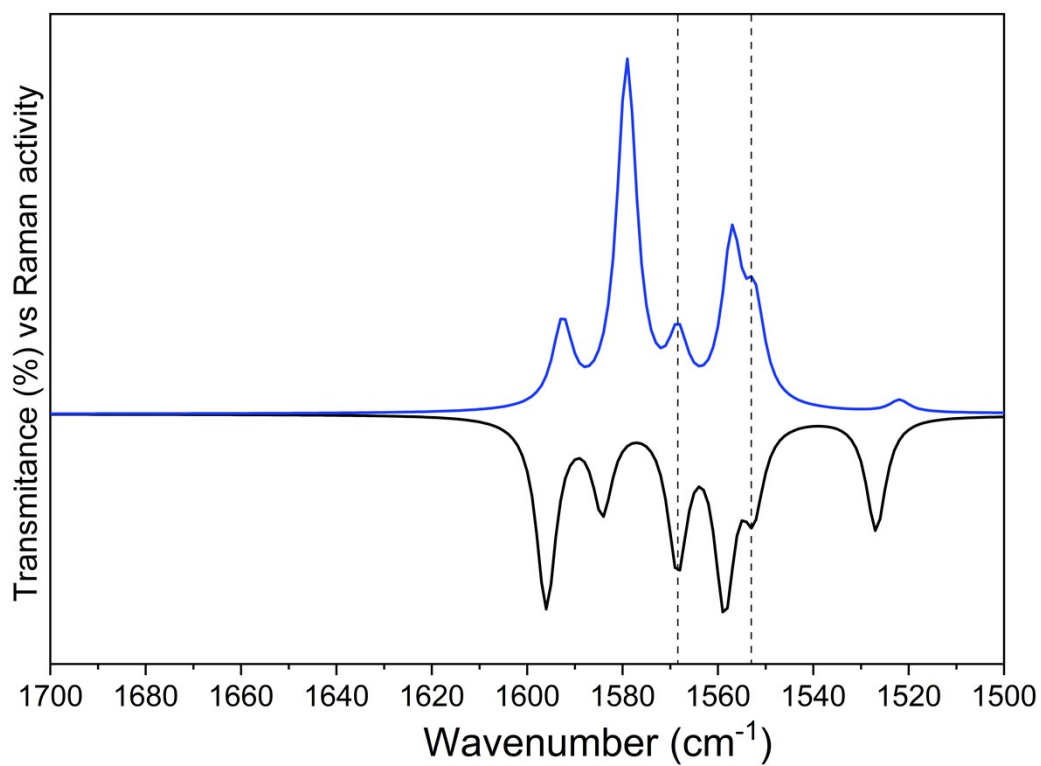


Figure S68. Comparison between theoretical Raman (blue line) and IR (black line) spectra at high (above) and low (below) energy of **TBQ2**. Bands are normalized to the strongest Raman and infrared bands.

S16. On surface chemistry methods

Experiments were performed in a custom-designed ultra-high vacuum system, with a base pressure below 5×10^{-10} mbar, hosting a commercial low-temperature scanning tunneling microscope STM from Scienta Omicron.

The Au(111) single crystal surface was prepared by repeated cycles of Ar⁺ ion sputtering ($E = 1.5$ keV) and subsequent annealing at 730 K for 10 minutes. **TBQ3** molecules were sublimated at 235 °C for 4 minutes, by using a Kentax TCE-BSC evaporator, onto the clean Au(111) surface kept at room temperature.

All shown STM images were taken in constant current mode, with a tungsten tip attached to a Q-plus tuning fork sensor functionalized with CO, at a sample temperature of 4.3 K. STM images were analyzed using WSxM.

S17. References

1. N. Martín, I. Pérez, L. Sánchez and C. Seoane, *J. Org. Chem.*, 1997, **62**, 870–877.
2. M. Yao, H. Sano, H. Ando, T. Kiyobayashi and N. Takeichi, *ChemPhysChem*, 2019, **20**, 967–971.
3. a) R. A. Abou-Elkhair and T. L. Netzel, *Nucleosides Nucleotides Nucleic Acids*, 2005, **24**, 85–110; b) K. Oyaizu, Y. Niibori, A. Takahashi and H. Nishide, *J. Inorg. Organomet. Polym.*, 2013, **23**, 243–250.
4. J. Yang, H. Su, Z. Wang, P. Sun and Y. Xu, *ChemSusChem*, 2020, **13**, 2436–2442.
5. G. R. Fulmer, A. J. M. Miller, N. H. Sherden, H. E. Gottlieb, A. Nudelman, B. M. Stoltz, J. E. Bercaw and K. I. Goldberg, *Organometallics*, 2010, **29**, 2176–2179.
6. Gaussian 16, Revision A.03, M. J. Frisch, G. W. Trucks, H. B. Schlegel, G. E. Scuseria, M. A. Robb, J. R. Cheeseman, G. Scalmani, V. Barone, G. A. Petersson, H. Nakatsuji, X. Li, M. Caricato, A. V. Marenich, J. Bloino, B. G. Janesko, R. Gomperts, B. Mennucci, H. P. Hratchian, J. V. Ortiz, A. F. Izmaylov, J. L. Sonnenberg, D. Williams-Young, F. Ding, F. Lipparini, F. Egidi, J. Goings, B. Peng, A. Petrone, T. Henderson, D. Ranasinghe, V. G. Zakrzewski, J. Gao, N. Rega, G. Zheng, W. Liang, M. Hada, M. Ehara, K. Toyota, R. Fukuda, J. Hasegawa, M. Ishida, T. Nakajima, Y. Honda, O. Kitao, H. Nakai, T. Vreven, K. Throssell, J. A. Montgomery, Jr., J. E. Peralta, F. Ogliaro, M. J. Bearpark, J. J. Heyd, E. N. Brothers, K. N. Kudin, V. N. Staroverov, T. A. Keith, R. Kobayashi, J. Normand, K. Raghavachari, A. P. Rendell, J. C. Burant, S. S. Iyengar, J. Tomasi, M. Cossi, J. M. Millam, M. Klene, C. Adamo, R. Cammi, J. W. Ochterski, R. L. Martin, K. Morokuma, O. Farkas, J. B. Foresman, and D. J. Fox, Gaussian Inc., Wallingford CT, **2016**.
7. A. V. Marenich, R. M. Olson, C. P. Kelly, C. J. Cramer and D. G. Truhlar, *J. Chem. Theory Comput.*, 2007, **3**, 2011–2033.
8. S. Miertuš, E. Scrocco and J. Tomasi, *Chem. Phys.*, 1981, **55**, 117–129.
9. A. D. Boese and J. M. L. Martin, *J. Chem. Phys.*, 2004, **121**, 3405–3416.
10. Z.-Z. Sun, S. Feng, C. Gu, N. Cheng and J. Liu, *Phys. Chem. Chem. Phys.*, 2019, **21**, 15206–15214.
11. R. Ditchfield, W. J. Hehre and J. A. Pople, *J. Phys. Chem.*, 1971, **54**, 724–728.
12. W. J. Hehre, R. Ditchfield and J. A. Pople, *J. Phys. Chem.*, 1972, **56**, 2257–2261.
13. P. C. Hariharan and J. A. Pople, *Theor. Chim. Acta*, 1973, **28**, 213–222.
14. V. A. Rassolov, M. A. Ratner, J. A. Pople, P. C. Redfern and L. A. Curtiss, *J. Comput. Chem.*, 2001, **22**, 976–984.
15. Y. Zhao and D. G. Truhlar, *Theor. Chem. Acc.*, 2008, **120**, 215–241.
16. J.-D. Chai and M. Head-Gordon, *Phys. Chem. Chem. Phys.*, 2008, **10**, 6615–6620.
17. N. Mardirossian and M. Head-Gordon, *Mol. Phys.*, 2017, **115**, 2315–2372.
18. A. D. Becke, *J. Chem. Phys.*, 1993, **98**, 5648–5652.

19. J. Autschbach and M. Srebro, *Acc. Chem. Res.*, 2014, **47**, 2592–2602.
20. NIST Computational Chemistry Comparison and Benchmark Database, NIST Standard Reference Database Number 101, Release 22, May 2022, Editor: Russell D. Johnson III, DOI:10.18434/T47C7Z; <http://cccbdb.nist.gov> (accessed March 2023).
21. M. Pérez-Escribano, J. Calbo and E. Ortí. (2023). TBAQ, TCAQ and TBQ1-5 structures predicted at the BMK/6-31G(d,p) (+PCM) level of theory [Data set]. Zenodo. <https://doi.org/10.5281/zenodo.8038098>
22. E. Ortí, R. Viruela and P. M. Viruela, *J. Mater. Chem.*, 1995, **5**, 1697–1705.
23. E. Ortí, R. Viruela and P. M. Viruela, *J. Phys. Chem.*, 1996, **100**, 6138–6146.
24. D. Kozłowski and J. Pilmé, *J. Comput. Chem.*, 2011, **32**, 3207–3217.